Title

Accelerated signal propagation speed in human neocortical microcircuits

Short title: Signal propagation in human microcircuits

Authors

Gáspár Oláh[1†], Rajmund Lákovics[1†], Sapir Shapira[2†], Yoni Leibner[2], Attila Szűcs[3], Pál Barzó[4], Gábor Molnár[1*], Idan Segev[2*], Gábor Tamás[1*]

Affiliations

[1] ELKH-SZTE Research Group for Cortical Microcircuits, Department of Physiology, Anatomy and Neuroscience, University of Szeged, Szeged, Hungary

[2] Edmond and Lily Safra center for Brain Sciences, The Hebrew University of Jerusalem, Jerusalem, Israel

[3] Department of Physiology and Neurobiology, Institute of Biology, Eötvös Loránd University, Budapest, Hungary

[4] Department of Neurosurgery, University of Szeged, Szeged, Hungary

[†]: These authors contributed equally.

*: Equal contribution of senior authors, correspondence: gtamas@bio.u-szeged.hu

Abstract

Human-specific cognitive abilities depend on information processing in the cerebral cortex, where neurons are significantly larger and sparser compared to rodents. We found that, in synaptically-connected layer 2/3 pyramidal cells (L2/3 PCs), soma-to-soma signal propagation delay is similar in humans and rodents. Thus, to compensate for the increase in neurons' size, membrane potential changes must propagate faster in human axons and/or dendrites. Dual somato-dendritic and somato-axonal patch recordings show that action potentials (APs) propagation speed is similar in human and rat axons, but the forward propagation of the EPSPs and the back-propagating APs are ~1.7-fold faster in human dendrites. Faithful biophysical models of human and rat L2/3 PCs, combined with pharmacological manipulations of membrane properties, showed that the larger dendritic diameter, combined with differences in cable properties, underlie the accelerated signal propagation in human cortical circuits. The implication for information processing in the human brain are discussed.

Teaser

Large human cortical neurons increase dendrite diameter and signal propagation speed for fast cell-to-cell communication.

MAIN TEXT

Introduction

The human neocortex is thought to be one of the most complex biological structures yet most of our knowledge regarding the properties of individual cortical neurons and their synapses is based on experiments performed in model organisms. Recent findings in human specimens indicated the emergence of new cell types in the human neocortex (*1–5*) and species related differences in transmitter release probability (*6*), regenerative dendritic events (*7–9*), ion channel composition of the dendrites (*10*), temporal dynamics of synaptic potentiation (*11*) and activity patterns of the microcircuits (*12–14*). Pioneering experiments indicate that human dendrites could evolve in ways favoring mechanisms not yet found in other species (*7, 9*) and might contribute to the apparent efficacy of human cognitive performance (*15*). Functional differences are accompanied by a divergence in morphological features, ranging from general alterations in the thickness of cortical layers to increasing complexity in anatomical properties of classical cell types(*5, 16*). Human pyramidal cells with larger and more extensively branching dendritic trees have an opportunity to receive higher number of synaptic inputs (*17–19*). This, when combined with the increase morphological complexity, endows human cortical neurons with enhanced computational and encoding capabilities (*5, 8*).

However, the increase in size of dendrites and axons might come with a cost of longer signal propagation times of both synaptic potentials in dendrites (larger dendritic delay) as well as action potentials in axons (axonal delay). This will slow down information processing, both within individual cortical neurons as well as in respective cortical circuits (*20, 21*). Indeed, transferring large amounts of information within and between brain regions in a short amount of time, and the capability of the neuronal circuit to respond sufficiently fast to its environment, is an important evolutionary function of neuronal networks (*21, 22*). Increased cell-to-cell delay will also affect plasticity/learning processes that depend on the timing between the pre- and the post-synaptic action potentials, e.g., the spike-timing-dependent plasticity (STDP) mechanism. It was therefore suggested that certain scaling morphological rules must be applied so that animals with larger brains can still function adequately in their environment (*23*). Is that the case for cortical neurons in human?

We set out in this study to directly measure the speed of signal propagation in both dendrites and axons of individual human and rat L2/3 pyramidal cells and applied experiments-based models to identify cellular and subcellular properties involved in controlling neuron-to-neuron propagation delays. Our integrative experimental and modeling study provides new insights into the scaling rules that enable to preserve information processing speed albeit the much larger neurons in the human cortex.

Results

Signal propagation paths and delays in human and rat pyramid to pyramid connections

We followed recent results indicating differences in the density and size of human and mouse supragranular pyramidal cells (PCs) (*4*) in a human-rat setting. As expected, measurements on 3D reconstructions based on randomly selected, electrophysiologically recorded and biocytin filled human (n=30) and rat (n=30) L2/3 cortical pyramidal cells (Fig. 1A) show significant differences in the horizontal (463.17 ± 119.48 vs. 324.79 ± 80.58 µm, *t* test: $P = 1.687 \times 10^{-6}$) and vertical extensions (542.58 ± 146.89 vs. 409.99 ± 102.69 µm, *t* test: P = 0.00013), and in the total dendritic (9054.94 ± 3699.71 vs. 5162.68 ± 1237.71 µm, *t* test: $P = 7.203 \times 10^{-7}$) and apical dendritic length (4349.76 ± 1638.39 vs. 2592.15 ± 818.26 µm, *t* test: $P = 1.638 \times 10^{-6}$, Fig. 1B,C).

To examine the temporal aspects of information propagation in excitatory microcircuits, we performed simultaneous whole cell patch clamp recordings in synaptically connected L2/3 PCs from acute neocortical slices from rat and human tissues (Fig. 2). Excitatory postsynaptic potentials (EPSPs) were measured in response to single action potentials (AP) in presynaptic cells (Fig. 2B). Synaptic latency was calculated as the time difference between the peak of the presynaptic AP and the onset point of the postsynaptic EPSP (see Methods). We did not find significant differences in synaptic latencies between human and rat PC-to-PC connections (rat: 1.198 ± 0.361 ms, n = 5; human: 1.175 ± 0.301 ms, n = 8; two-sample *t* test: P=0.905, Fig. 2C). Both pre- and postsynaptic PCs were filled with biocytin during recordings allowing for post hoc identification of close appositions between presynaptic axons and postsynaptic dendrites (Fig. 2A). We measured the shortest axonal path lengths linking the presynaptic soma to close appositions on the postsynaptic dendrite (rat: 78.36 ± 13.86 µm, human: 120.975 ± 37.55 µm) and the shortest dendritic path lengths from close appositions to the postsynaptic soma (rat: 176.22 ± 47.2 µm, human: 264.5 ± 63.15 µm). Consequently, we found that the minimal intersomatic distance (the sum of the shortest axonal and dendritic paths) in each synaptically connected PC-to-PC pair was significantly smaller in rats compared to humans (rat: 262.22 ± 53.639 µm, human: 385.7 ± 74.277 µm, two-sample t-test: P=0.008, Fig. 2D). Given that similar synaptic latencies accompany different lengths for signal propagation in the two species, membrane potentials (APs and/or EPSPs) must propagate faster in human PC-to-PC connections.

Direct measurements of signal propagation in PC dendrites and axons

Compensation of longer axonal and dendritic paths must be explained by higher velocity of signal propagation along axons and/or along dendrites. We therefore asked whether interspecies differences can be found in axonal and/or dendritic signal propagation in L2/3 PCs. We first sought to test rat and human dendritic signal propagation velocity using simultaneous somatic and dendritic whole cell patch clamp recordings. Distances of somatic and dendritic recording locations (rat: n=23, 127.06 ± 69.48 µm vs. human: n=39, 151.74 ± 62.29 µm) were chosen to be similar in the two species (Mann-Whitney test: p=0.07543, Suppl Fig. 1A) and in range of soma-to-dendrite distances of axo-dendritic close appositions determined above for synaptically coupled PC-to-PC connections. In the first set of experiments, we injected suprathreshold current through the somatic electrode and measured the time difference between the evoked AP at the soma and the respective backpropagating AP in the dendritic electrode (Fig. 3A and B). We found significant difference in the signal propagation time between rat and human PCs (rat: 407.35 ± 162.39 µs, n = 23; vs. human: 314.27 ± 153.97 µs, n = 39, Mann-Whitney test: P = 0.0304, Fig. 3B). The AP propagation speed was calculated for each cell from the time difference between the somatic and dendritic APs divided by the distance between the two points. We found that the propagation speed was, on average, ~1.7-fold faster in human (rat: 0.31 ± 0.1 m/s vs. human: 0.53 ± 0.16 m/s, Welch's *t*-test: P = 2.691×10^{-8}, Fig. 3B). In a second set of experiments, using the same dual recording configuration, we tested orthodromic or forward propagating signal propagation velocity by injecting subthreshold simulated EPSP signals in the dendrites and recorded the resultant voltage response in the soma (Fig. 1C). These experiments were performed in the same PCs where backpropagating AP velocity where also measured (rat: n = 6, human: n = 5). Signal propagation time (latency) of EPSPs were similar in rat and human PCs (rat: 382.33 ± 270.64 µs vs. human: 420.75 ± 198.12 µs, Mann-Whitney test: P = 0.477; Fig. 3D). We found that EPSP propagation speed was, on average, ~1.6-fold faster in human (rat: 0.312 ± 0.054 m/s vs. human: 0.435 ± 0.138 µs, Mann-Whitney test: P = 0.045; Fig. 3D).

Next, we investigated whether we can find dissimilarities between the two species in the speed of signal propagation along axons of PCs. We whole cell recorded the soma and a distal axon simultaneously, positioning the axonal recording electrode on one of the blebs formed at the cut

ends of axons during slice preparation. Somatic current injections were used to trigger APs and the time between somatic and the axonal AP was measured (Fig. 3E). We captured two-photon images during electrophysiological recording and measured the length of the axonal path from the somatic to the axonal electrode on image z-stacks. The dataset was restricted to recordings that were made on axons longer than 150 µm, in agreement with distances from the soma to axo-dendritic close appositions determined above along the axon of synaptically coupled PC-to-PC connections. The axonal speed of AP propagation was calculated for each cell from the time required from soma to recording site. We did not find significant difference the propagation speed of APs in the axons of rat and human (rat: n = 8, 1.214 ± 0.419 m/s vs. human: n = 9, 1.492 ± 0.583 m/s, two sample *t*-test: P = 0.282, Fig. 3F).

Contribution of experimentally determined properties of pyramidal cell dendrites to signal propagation velocity

Our simultaneous soma-dendritic and soma-axonal recordings suggest that dendritic properties have significant contribution to interspecies differences in signal propagation velocity. Anatomical features of neuronal processes have a major influence on signal propagation properties (*5, 20*), thus, in addition to the soma-dendritic path measurements shown above, we also measured the thickness of dendrites at every 0.5 µm along the path linking the somatic and dendritic electrodes on two-photon image stacks captured during electrophysiological measurements (Fig. 4A-C). We found that the mean diameter of dendrites was thicker in human (n = 38, 1.07 ± 0.274 µm) compared to the rat (n = 23, 0.899 ± 0.148 µm, Mann-Whitney test: P = 0.0169, Fig. 4D). Moreover, in samples where we acquired both dendrite thickness and bAP signal propagation velocity, we found that the cross-section area of dendrites was correlated with the speed of backpropagating APs (Fig. 4E).

In addition to dendritic thickness, we also tested potential effects of active dendritic conductances on signal propagation speed. Hyperpolarization-activated cyclic nucleotide-modulated (HCN) channel densities were shown to be higher in human compared to rat layer 2/3 PCs and were shown to be instrumental in more depolarized resting membrane potentials and in larger sag potentials in response to hyperpolarization in the human (*10*). In addition, modeling predicted that signal delay in dendrites reduces with increased h-conductance (*10*). In line with previous studies, human PCs in our dataset had more depolarized resting membrane potential (rat: -69.89 ± 0.50 mV, n = 23, human: -66.05 ± 0.68 mV, n = 36, Mann-Whitney test: P = 0.01854, Suppl.fig. 1B) and lower somatic input resistance (rat: 69.94 ± 22.56 MΩ, n = 23, human: 59.79 ± 44.35 MΩ, n = 36, Mann-Whitney test: P = 0.00292, Suppl.fig. 1C). To test the contribution of h-channels to the elevated signal propagation speed in human dendrites, we performed pharmacological experiments with 20 µM ZD7288, a specific blocker of h-channels. Significant hyperpolarization of the resting membrane potential and increased input resistance accompanied drug application in both human and rat neurons (Suppl.fig. 2A). Drug application significantly decreased bAP propagation speed in human PCs (control: 0.486 ± 0.108 m/s, ZD7288: 0.466 ± 0.067 m/s, n = 8, Wilcoxon signed ranks test: P = 0.014, Fig. 5B) but not in rat PCs (control: 0.285 ± 0.067 m/s, ZD7288: 0.267 ± 0.078 m/s, n = 9, paired *t* test: p = 0.104, Fig. 5A). Along the same vein, changes in bAP propagation speed were higher in the human cells (rat: -0.018 ± 0.029 m/s, human: -0.06 ± 0.04 m/s, two-sample *t* test: P = 0.029, Fig. 5C) in response to h-channel blockage.

Back-propagation of APs is an active process supported by voltage gated ion channels that can initiate regenerative events in the dendrites (*24*). To further investigate the influence of voltage gated ion channels we pharmacologically blocked voltage gated Na^+ channels with tetrodotoxin (TTX, 1µM), voltage gated Ca^{2+} channels with cadmium chloride ($CdCl_2$, 200 µM), and NMDA

receptors with (2*R*)-amino-5-phosphonovaleric acid (AP5, 20 µM), simultaneously. Since the blockage of voltage gated Na^+ channels prevents the initiation of APs, we kept the soma of the recorded cells in voltage clamp mode and used a prerecorded template as voltage command through a somatically placed electrode (the so called "simulated spike") and measured the back propagation of the response to the somatic voltage command at a dendritic recording site in current clamp mode. As expected, the amplitude of the bAPs at the dendritic recording site dropped significantly in human and rat cells respectively (Suppl.fig. 3). The speed of back propagation of membrane potential signals in dendrites turned "passive" by the pharmacological cocktail was significantly lower compared to drug-free control both in rat and human samples (rat control: 0.3622 ± 0.061 m/s, rat TTX/$CdCl_2$/AP5: 0.194 ± 0.071 m/s, paired *t* test: P = 6.101×10^{-6}, human control: 0.565 ± 0.144 m/s, human TTX/$CdCl_2$/AP5: 0.425 ± 0.123 m/s, paired *t* test: P = 7.739×10^{-6}, Fig. 5D,E). However, changes in bAP propagation speed in response to the pharmacological cocktail were similar in human and rat cells suggesting a combined equal contribution of Na^+, Ca^{2+} and NMDA channels (Fig. 5F). Moreover, human dendrites made "passive" by the cocktail retained higher bAP propagation speed (rat: 0.194 ± 0.071 m/s n=8, human: 0.425 ± 0.123 m/s n = 8, two sample *t* test: P = 4.244×10^{-4} Fig. 5G). Taken together, when searching for factors contributing to higher signal propagation speeds in human compared to rat pyramidal dendrites, passive properties seem to have a major role in differentiating the two species and these are supplemented by minor contribution from voltage gated ion channels (eg. HCN channels) having different densities in human vs. rat.

Effect of cell membrane capacitance

The specific membrane capacitance (C_m) can influence the time constant of the biological membrane, and it is a key determinant of the propagation of electrical signals. Recent experiments indicated that the C_m of human L2/3 PCs might be significantly lower compared to rodents (*25*) and modeling studies suggested that the decrease in C_m could lead to increased conduction speed and fewer synapses being able to evoke suprathreshold events in human PCs (*25*). However, a separate line of experiments could not detect differences in the C_m of L5 PCs between humans and rodents (*7*), thus, to test whether C_m is a component in producing elevated signal propagation velocity in human dendrites, we directly measured the C_m values of human and rat PCs by pulling nucleated patches (*25*) (Fig. 6A,B). We found no significant difference in the C_m between the human and rat L2/3 PCs (rat: 1.092 ± 0.14 µF/cm^2 n = 20; human: 0.987 ± 0.196 µF/cm^2 n = 19, two-sample *t* test: P = 0.0615, Fig. 6C). The specific membrane capacitance is determined by the dielectric constant of the membrane, and it is inversely proportional with the membrane thickness. We measured the membrane thickness of dendritic structures with transmission electron microscopy both in human and rat samples (Fig. 5D,E) and detected no significant differences between the two species (human: 4.271 ± 0.873 nm, n = 213 from n = 3 patient; rat: 4.122 ± 0.779 nm n = 151 from n = 3 rat, Mann-Whitney test: P = 0.212, Fig. 6E).

Models show faster EPSP propagation in dendrites of human pyramidal cells

Detailed compartmental models were utilized to disassemble the effect of various morphological and cable parameters on the latency and velocity of synaptic potential in human and rat L2/3 dendrites. Based on the 3D morphological reconstructions of five human and two rat PCs, we first asked, how morphological differences per se affect signal propagation, assuming that the cable parameters (C_m = 1 $\mu F/cm^2$, R_m = 15,000 Ωcm^2, R_a = 150 Ωcm) are identical in all cells (Fig. 7). Figure 7A shows EPSPs latency as a function of the distance from its dendritic initiated site and the soma. Latency was calculated as the time difference between local dendritic EPSP peak and the resulting EPSP peak at the soma. For the cable parameters used, the latency ranges between 0.1 - 8 ms for the rats (red circles) and between 0.01 – 25 ms in humans (blue). This difference is

partly due to the difference in dendritic length between the two species, which are about 3-folds longer in humans. Focusing on the range of distances in which the experiments were performed (rectangle at lower left) we found that, for an identical physical distance from the soma, EPSPs latency in rats was larger compared to humans.

To further validate this, we computed the mean latency as a function of distance from soma, averaged over the latency across different branches in a given distance from the soma (lower right inset). Indeed, the latency is larger in rat versus human. For example, at a distance of 288 μm from the soma, the average latency in rat neurons was about 5.9 ms and only 4.4 ms in humans. In Fig. 7B we computed the EPSPs velocity, calculated by dividing the distance of the dendritic site of EPSP origin from soma by its latency. EPSPs velocity in human PCs ranges between 0.016 - 0.5 m/s, versus 0.026 - 0.09 m/s in rat, with higher velocity in human compared to rats for every respective distance point (inset).

A possible reason for the smaller latency and larger velocity of EPSPs in human dendrites is that they are thicker than in rats (Figs. 4D and Fig. 7C). Indeed, theory shows that, if all other electrical parameters are fixed, larger dendritic diameter will result in faster signal propagation (see below). For infinitely long passive cylindrical cable, the velocity of passive signals is fast near their site of origin, converging to a value of $2\lambda/\tau$ away from the initiation point. λ is the space constant and τ the membrane time constant (*26, 27*). This means that, if we normalize the physical distance, x, by λ (which is $\propto \sqrt{d}$, where d is the cable diameter) and all cable parameters are identical, then the velocity (in units of λ) of passive signals will be identical in infinitely long cylindrical cables with different diameters (see Suppl Fig. 4). Hence, after normalizing the distance in cable units, we expect that the circles in Fig. 7A,B will fall on similar curves (this normalization does not take into account local impedance mismatch due to local diameter change, e.g., at branch points, see Suppl Fig. 5 and Discussion).

To explore the effect of dendritic diameters in human versus rat on EPSPs latency and velocity, we therefore normalized in Figs. 7D and 7E the distance in units λ. indeed, with this normalization, both latency (Fig. 7D) and velocity (Fig. 7E) are more similar across all seven cells modeled (compare Fig. 7D,E to Fig. 7A,B, respectively). Thus, differences in velocity and latency are correlated with dendritic diameter along the path between dendritic location of EPSP initiation and the soma. However, we find strong variability in latency and velocity, both before (Fig. 7A,B) and after normalization of distance in units of λ (Fig. 7D,E), both within the same PC as well as between PCs. Thus, our results show that local morphological variability within and between cells give rise to variability in EPSP velocity (and latency), even for dendritic locations that are at the same cable distance from the soma. Moreover, our simulations show that, in the normalized case, EPSP velocity originated in the dendrites is reduced as it approaches the soma (Fig. 7E). Indeed, the boundary conditions (the conductance load imposed by the soma and basal dendrites on EPSPs arriving from the apical tree) add another morphological effect on signal propagation in dendrites (*27*). Indeed, several simplified models that we constructed with uniform cable parameters but variable morphologies, show that mere morphological irregularities and different boundary conditions have strong effects on signal propagation in dendritic cables (Suppl Fig. 5). To summarize the results of this part of the study, Figure 7F uses a “latency-gram” to graphically compare the latencies expected in human versus rat dendrites when all cable parameters are uniform as assumed above.

Each of the three key passive parameters: the specific membrane resistivity and capacitance (R_m, C_m) and the specific axial resistivity, R_a, can either exaggerate or reduce the morphological effects on signal propagation properties in dendrites. Thus, we further asked how the actual specific parameters of the various PCs studied affect signal propagation in their respective dendrites.

Toward this end, we fitted cable parameters individually to each of the 7 PCs. Figure 8A shows an exemplar human L2/3 PC reconstruction with the locations of the two recordings/stimulation electrodes used in the experiments for this cell. Figure 8B top shows the case where the injected current was at the dendrite (cyan); the resultant voltage is depicted below in cyan, the model fit in superimposed dark blue (D-to-S direction). The opposite (S-to-D) direction is depicted by the next three traces below. This fit enables a direct estimate of the cable parameters per cell. The results are depicted in Table 1.

Figure 8C-F extends the simulations shown in Figure 7A,B,D,E, but with the fitted (rather than uniform) cable parameters per cell. Compared with the uniform case, the latency and propagation velocity differences between and within the two species are enhanced (compare Fig. 8C,D to Fig. 7A,B). For the per cell fit, the latency ranges between 0.1 - 9 ms for rats (red) and 0.1 – 28 ms in humans (Fig 8C) and the velocity ranges between 0.03 - 0.08 m/s for rats (red) and 0.02 – 0.8 m/s in humans (Fig 8D). In Figures 8E and 8F, the distance was normalized by the space and time constants calculated per cell. After normalization, both latency (Fig. 8E) and velocity (Fig. 8F) are much more similar across all models; however differences among individual cells are larger compared with Figure 7D,E where uniform cable parameters were assumed.

Zooming in to the experimental regime of dendritic measurements (inset) shows the smaller latency and faster velocity in human versus rat (Fig. 8C,D, respectively). Quantifying the differences between human and rat PCs within this regime (Table 2), latency of EPSPs in human PCs is 1.75 times smaller on average compared to rats (4.12 ms in humans versus 7.02 ms in rats, Table 2). While the average time constants of the two species are similar (11.84 ms in humans versus 10.75 ms in rats, Table 2); the cable length of human PCs dendrites is 1.6 smaller than that of rats (0.81 in human and 1.29 in rats, Table 2), mostly due to the larger dendritic diameter in humans (0.9 μm in humans versus 0.32 μm in rats at ~288 μm distance from soma, Table 2), but it is further emphasized due to differences in specific cable parameters between humans and rats neurons (See Suppl Table 2, as compared to the case with uniform cable parameters). Indeed, in our set of extracted cable parameters, R_m is on average 1.6 larger in humans (17,266 versus 11,097 Ωcm^2) whereas R_a is 1.3 time smaller in human (203 Ωcm versus 258 Ωcm) and C_m is 1.45 times smaller in humans (0.69 versus 1.00 $\mu F/cm^2$; see Table 1). The effect of these differences on of signal propagation in human versus rat dendrites will be elaborated in the Discussion.

We summarize this section by noting that our modeling effort enabled the dissection of morphological and electrical parameters that affect differences in EPSPs velocity and latency between humans versus rats L2/3 PCs' dendrites. By first assuming uniform cable properties for all cells' modeled (Fig. 7) we found that the larger diameter of the proximal apical dendrite in humans has two cumulative consequences. (i) Human synapses are electrotonically closer to the soma (and therefore have shorter distance to travel to it) and (ii) Because EPSPs velocity is high near their site of origin (decreasing to $2\lambda/\tau$ with distance from this site), the electrotonically closer EPSPs in humans have higher initial velocity (shorter latency) for synapses located at the same physical distance to the soma. In Figure 8 we next fitted cable parameters for the 7-experimentally measured and 3D reconstructed cells. This enables us to show the effect of dendritic diameter on EPSPs propagation in humans versus rats which is further exaggerated due to differences in specific cable properties. This will be further elaborated in the Discussion.

Discussion

Emergence of data concerning conserved and divergent features of different mammalian species in the structure and function of the cerebral cortex suggest fundamental similarity across species (*28–30*) with a subset of specialized features documented in the human cortex. A number of these

specialized properties, like the increase in the size of individual neurons detected early by Ramón y Cajal (*31*), have far reaching functional consequences and here we identified some compensatory mechanisms which, in turn, are based on additional specialized features. In particular, we studied propagation velocity of both forward (axonal) and backward (dendritic) action potential, as well as of EPSPs in human and rat dendrites. Our experimentally-based models showed that the average membrane time constant of the two species is similar (~11 ms). Yet, EPSPs arising in the apical dendrite at similar distances from the soma have significantly shorter latency in humans. This results primarily from the larger diameter of the apical trunk in humans, but also from the difference in cable properties between the two species.

Detailed compartmental models of 3D reconstructed and biophysically measured L2/3 PCs of human and rat L2/3 PCs enabled us to systematically explore factors affecting EPSPs propagation speed in dendrites of these two species. Since the dendritic diameter is larger in human, and assuming that all specific cable parameters were identical, a synapse located at a given physical distance from the soma is electrotonically closer (in units λ) to the soma in human. Consequently, the EPSP latency is expected to be shorter in human dendrites. This shorter cable distance of the human synapse has an additional consequence. The velocity of the EPSP peak in dendrites is not constant; it is faster near the synapse, converging to a constant value of 2λ/τ with distant from the synapse (see Suppl Fig. 5 and (*27*) Therefore, EPSPs originated at electrotonically closer synapses fall on the faster phase of their velocity curve, implying a shorter latency to the soma. A third factor affecting the faster EPSPs propagation in human, results from difference in their respective specific cable parameters. We found that the membrane time constant, τ, is ~1.1 larger in human (Table 1). $\lambda = \sqrt{(d/4)R_m/R_a}$ and Table 1 shows that the average axial resistivity, R_a, is 1.3 time smaller in human and R_m is 1.6 larger in humans. Thus, $\sqrt{R_m/R_a}$ is 1.44 larger in human L2/3 PCs. Taken together, and under the infinite cable assumption, differences in specific cable parameters *per se* result in enhancing EPSP propagation speed in human dendrites by a factor of 1.44/1.1 = 1.31. This contribution of specific cable parameters to increase in signal velocity in human neurons can be appreciated by contrasting the case with uniform to the case with specific cable parameters (Figs. 7 and 8 and Table 2 and Suppl Table 2). Additional factors, such impedance mismatch due to local morphological irregularities at branch points and in dendritic spines, might play an additional role in affecting signal propagation speed (*32*). These possibilities will be explored in a future study.

It was recently suggested that axonal structure optimizes signal propagation delay under constraints such as metabolic cost and limited brain volume (*22, 33*) and that, in contrast, the key principle governing dendritic structure is reducing passive cable attenuation rather than conduction time delay (*34, 35*). Our results, however, demonstrate that both voltage attenuation and conduction delay are reduced in the larger cortical human dendrites through an increase in dendritic diameter combined with changes in specific cable properties (resulting in increasing the dendritic space constant, λ). Importantly, we have found that the membrane time constant, τ, is similar in L2/3 PCs of rodents and human implying the preservation of coincidence detection capabilities of dendrites in both species. This is important because coincidence detection in dendrites is a fundamental mechanism for a variety of plasticity mechanisms and computational functions such as directional selectivity, sound localization and expansion of the dynamic range of sensory processing (*36–39*) and see review in (*40*).

Multifaceted upscaling of properties found in the human microcircuit is usually considered instrumental in functional enrichment. For example, increase in the number of human supragranular pyramidal cell types compared to the mouse (*4, 5, 16*) might help in separating multiple tasks of parallel processing in cortical circuits in and the increased range of synaptic

strength in pyramidal output contributes to increased saliency of individual excitatory cells followed by efficient network pattern generation in human (*6, 11, 14*). However, increase in the size and in morphological complexity of individual neurons might not follow a simple bigger is better logic, but instead it is rather a double-edged sword when considering cellular and microcircuit level function (*16, 20, 41–44*). On one hand, additional dendritic length can receive a higher number and a more diverse set of inputs contributing to circuit complexity (*18, 19*) and sophistication of dendritic architecture has been reviewed as the site for elaborate subcellular processing (*5, 8, 9, 16, 30*). On the other hand, signals need to propagate along a longer route through dendritic or axonal trees of increased size. Without compensatory mechanisms, textbook knowledge dictates that longer propagation times and altered waveforms of signals associate with elongated neural processes (*21, 22, 26, 27*). Our observation that soma-to-soma pyramidal cell synaptic latencies are similar in human and rodent strongly suggest that compensatory mechanisms evolved together with alterations in dendritic structure such as increased thickness of dendritic segments in the human compared to segments equidistant from the soma in the rat. This finding is backed up by earlier experiments showing similar soma-to-soma latencies between presynaptic pyramidal cells and postsynaptic fast spiking interneurons in human and rat (*6*) and between human and mouse pre-and postsynaptic cells overall in the neocortex (*45*). Thus, it appears that signals connecting pyramid-to-pyramid and pyramid-to-interneuron cell pairs have an evolutionally conserved latency and compensation provided by dendritic structure seems precise. Importantly, based on the datasets available, there is no indication of significant over/under-compensation and acceleration/deceleration of soma-to-soma propagation times.

Precision in monosynaptic latencies across species is instrumental in keeping the timeframe relatively stable for circuit plasticity. Research in animal models laid experimental and theoretical foundations and uncovered bewildering multiplicity of mechanisms explaining the induction and maintenance of plasticity in cortical microcircuits (*46–52*). In contrast, plasticity is understudied in human samples both at the cellular and microcircuit level (*53, 54*). Spike time dependent plasticity (STDP) is based on the relative timing of pre-and postsynaptic activity (*55–57*) and the paramount feature of STDP experiments to date is that minute jitter between pre- and postsynaptic activity results in major changes in synapse strength (*11, 58*). Pioneering STDP studies in human neurons showed a wide temporal STDP window with a reversed STDP curve compared to classic results detected in rodent brain (*11, 58*). Interestingly, dendritic L-type voltage-gated calcium channels were found important in human STDP rules (*11*), yet our results indicate that dendritic bAP speed is equally influenced by calcium channels in human and rat. However, the faster bAP propagation found here in human PCs is compatible with the shifted STDP rule switch (*11*) by allowing postsynaptic somatic action potentials to be generated later yet arriving to dendrites at the same time relative to presynaptic spikes. It remains to be established how altered cable properties reported here interact through a dynamic interplay between potentially human specific dendritic ion channel distribution and local dendritic regenerative processes in order to achieve the reversed STDP curve in human (*7–10, 41, 42*).

In addition to associative plasticity, precision of synaptic delays is crucial in the generation of circuit oscillations and network synchronization. Although all known patterns of local field potentials and behavioral correlates present in the human cortex can be detected in other mammals (*21*), fast oscillations are thought to be especially important in cognitive performance (*59–61*). Fast population rhythms in the cerebral cortex in the gamma and high gamma range are based on alternating activation of monosynaptically coupled and reciprocally connected pyramidal cells and interneurons (*62, 63*) and similar mechanisms were proposed for some forms of ripple oscillations (*12, 13, 63*). The relatively small axonal distances and accordingly short axonal AP propagation latencies linking locally connected human PCs and or interneurons found

here and earlier (*6, 11–13, 15, 45*) are compatible with the frequency range of fast oscillations. Brief loop times during sequential reactivation of a subset of closely located neurons participating in fast human rhythms are helped by subcellular placement of PC-to-PC (and PC-to-fast spiking interneuron (*6, 12*)) synapses on midrange dendritic segments instead of distal branches and by extremely effective glutamatergic synapses on interneurons triggering postsynaptic spikes in response to unitary input from a PC (*6, 12*) in addition to accelerated human dendritic signal propagation. Indeed, latencies of monosynaptic spike-to-spike coupling in single cell triggered Hebbian assemblies characteristic to the human cortical circuit are compatible with up to ~200 Hz frequency (*12, 13*). Phasic and sequential firing of interneurons and PCs was reported in vivo during fast oscillations in humans (*64*) and single cell spiking sequences emerging during human memory formation are replayed during successful memory retrieval (*65*) similar to results pioneered in the hippocampus of rodents (*66–68*). Our results suggest that changes in human dendritic properties contribute to cross species preservation of fast oscillation related cortical function at the local microcircuit level.

Materials and Methods

Experimental Design

Slice preparation

Experiments were conducted according to the guidelines of University of Szeged Animal Care and Use Committee (ref. no. XX/897/2018) and of the University of Szeged Ethical Committee and Regional Human Investigation Review Board (ref. 75/2014). For all human tissue material written consent was given by the patients prior to surgery. Human neocortical slices were sectioned from material that had to be removed to gain access for the surgical treatment of deep-brain target ($n = 23$ female and $n = 18$ male, aged 48.5 ± 17.8 years). Anesthesia was induced with intravenous midazolam and fentanyl (0.03 mg/kg, 1–2 µg/kg, respectively). A bolus dose of propofol (1–2 mg/kg) was administered intravenously. The patients received 0.5 mg/kg rocuronium to facilitate endotracheal intubation. The trachea was intubated, and the patient was ventilated with O_2/N_2O mixture at a ratio of 1:2. Anesthesia was maintained with sevoflurane at care volume of 1.2–1.5. Following surgical removal, the resected tissue blocks were immediately immersed into a glass container filled with ice-cold solution in the operating theater and transported to the electrophysiology lab. For animal experiments we used the somatosensory cortex of young adults (19–46 days of age, (P) 23.9 ± 4.9) male Wistar rats. Before decapitation animals were anesthetized by inhalation of halothane. 320 µm thick coronal slices were prepared with a vibration blade microtome (Microm HM 650 V; Microm International GmbH, Walldorf, Germany). Slices were cut in ice-cold (4°C) cutting solution (in mM) 75 sucrose, 84 NaCl, 2.5 KCl, 1 NaH_2PO_4, 25 $NaHCO_3$, 0.5 $CaCl_2$, 4 $MgSO_4$, 25 D(+)-glucose, saturated with 95% O_2 and 5% CO_2. The slices were incubated in 36°C for 30 min, subsequently the solution was changed to (in mM) 130 NaCl, 3.5 KCl, 1 NaH_2PO_4, 24 $NaHCO_3$, 1 $CaCl_2$, 3 $MgSO_4$, 10 D(+)-glucose, saturated with 95% O_2 and 5% CO_2, and the slices were kept in it until experimental use. The solution used for recordings had the same composition except that the concentrations of $CaCl_2$ and $MgSO_4$ were 3 and 1.5 mM unless it is indicated otherwise. The micropipettes (3–5 MΩ) were filled (in mM) 126 K-gluconate, 4 KCl, 4 ATP-Mg, 0.3 GTP-Na_2, 10 HEPES, 10 phosphocreatine, and 8 biocytin (pH 7.25; 300 mOsm).

In vitro electrophysiology

Somatic whole-cell recordings were obtained at ~37°C from simultaneously recorded PC-PC cell pairs visualized by infrared differential interference contrast (DIC) video microscopy at depths 60–160 µm from the surface of the slice (Zeiss Axio Examiner LSM7; Carl Zeiss AG, Oberkochen, Germany), 40× water-immersion objective (1.0 NA; Carl Zeiss AG, Oberkochen, Germany) equipped with Luigs and Neumann Junior micromanipulator system (Luigs and Neumann, Ratingen, Germany) and HEKA EPC 10 patch clamp amplifier (HEKA Elektronik GmbH, Lambrecht, Germany). Signals were digitalized at 15 kHz and analyzed with custom written scripts in Python.

Presynaptic cells were stimulated with a brief suprathreshold current paired pulse (800 pA, 2–3 ms, 50-60 ms separation of the two pulses), derived in 10s interval. The postsynaptic cells were recorded in current-clamp recording, holding current was set to keep the cell's membrane potential around −50 mV. The experiments were stopped if the series resistance (Rs) exceeded 35 MΩ or changed more than 20%.

For the dendritic recordings 20µM Alexa 594 was added to the internal solution of the somatic pipette and 20 µM Alexa 488 to the internal solution of the dendritic pipette. The PCs were kept in whole cell configuration at least 10 minutes before the axon bleb or dendritic targeted recording started. Then the microscope switched to 2p mode. The fluorescent dyes of the pipette solution were excited at 850 nm wavelength with a femtosecond pulsing Ti:sapphire laser (Mai Tai DeepSee, Spectra-Physics, Santa Clara, CA). The axon blebs and the dendrites were targeted in 2p mode. After the successful seal formation, the imaging was switched off to reduce the phototoxicity in the sample. All the recordings were carried out in current clamp mode. 800ms long square pulses with elevating amplitude (from -110 to 300 pA) were used to evoke APs. In some experiments the same long square injection protocol was repeated at the dendritic/axonal recording site. For measuring the forward propagation of electrical signals in dendrites, we applied a short triangle current injection to the through the dendritic pipette. 10 minutes of recording we applied different drugs or finished the recordings. At the end of the recording, we acquired a 2p Z series from the recorded dendrite. Then the pipettes were carefully withdrawn from the cells. The slices went under chemical fixation for further anatomical investigation.

The specific membrane capacitance recordings were carried out as described previously[15,16]. Briefly, the L2/3 PCs were whole cell patch clamped, and a gentle suction made during slow withdrawal of the pipette. The nucleus of the cells were pulled out and the voltage clamped at -70 mV. -5mV voltage steps (repeated 100 times) were applied and the capacitive transients were measured. A DIC image of the nucleus were made for calculation of the membrane surface with the following equation:

$$(1) A = \frac{(a+b)^2 * \pi}{4}$$

Where a is the shorter diameter of the ellipse and b is the longer one. After the recording the nucleus was blown away and the pipette tip was pushed into a sylgard ball until the GOhm seal formed. The -5 mV voltage steps were applied again to record the residual capacitance of the system. Before the analysis we subtracted the residual capacitance from the transients.

Pharmacological experiments were carried out on PCs during simultaneous somatic and dendritic recordings after 10 minutes of control recording using ACSF with the following drugs: 20 µM 4-(*N*-ethyl-*N*-phenylamino)-1,2 dimethyl-6-(methylamino)pyrimidinium chloride (ZD7288) (Sigma-Aldrich), or 1 µM TTX, 200 µM $CdCl_2$, and 20 µM AP5.

Post hoc anatomical analysis of recorded cell pairs

After electrophysiological recordings, slices were fixed in a fixative containing 4% paraformaldehyde, 15% picric acid, and 1.25% glutaraldehyde in 0.1 M phosphate buffer (PB; pH = 7.4) at 4°C for at least 12 hr. After several washes in 0.1 M PB, slices were cryoprotected in 10% then 20% sucrose solution in 0.1 M PB. Slices were frozen in liquid nitrogen then thawed in

PB, embedded in 10% gelatin, and further sectioned into slices of 60 µm in thickness. Sections were incubated in a solution of conjugated avidin-biotin horseradish peroxidase (ABC; 1:100; Vector Labs) in Tris-buffered saline (TBS, pH = 7.4) at 4°C overnight. The enzyme reaction was revealed by 3'3-diaminobenzidine tetrahydrochloride (0.05%) as chromogen and 0.01% H_2O_2 as an oxidant. Sections were post-fixed with 1% OsO_4 in 0.1 M PB. After several washes in distilled water, sections were stained in 1% uranyl acetate, dehydrated in an ascending series of ethanol. Sections were infiltrated with epoxy resin (Durcupan, Sigma-Aldrich) overnight and embedded on glass slices. 3D light microscopic reconstructions were carried out using the Neurolucida system with a 100× objective. The number of putative synaptic contacts were determined by searching for close appositions of presynaptic axon terminals and postsynaptic dendrites under light microscopy. The distance of the contact sites alongside the branches were measured with Neurolucida. The intersomatic distance was calculated from the branch length from the presynaptic soma to the putative synaptic contact alongside the axon, and the length of the dendrite from the contact site to the postsynaptic soma. If there were more than one putative synapse between the cells, we took the shortest intersomatic path distance for that given cell pair.

Electron microscopy

Sample preparation for the electron microscopy were performed as described previously (*2*). Briefly, digital images of serial EM sections (20 nm thickness) were taken at 64 000x magnification with a FEI/Philips CM10 electron microscope equipped with a MegaView G2 camera. The membrane thickness measurements were carried out on digital images with a custom software. Briefly, postsynaptic dendritic structures were identified with the presence of postsynaptic densities (PSD) faced in front of axon terminals filled with vesicles. At least 20 nm away from the PSD perpendicular lines were used as region interests (ROI). The intensity line profile of each ROI was calculated, and edge detection was carried out on them. The thickness was determined as the distance between the first and last point along the line profile where the gradient magnitude was larger than 50.

Data analysis

The electrophysiological recordings were analysed by custom written python scripts. First the recorded sweeps were exported with HEKA FitMaster to ascii files. The synaptic delay in the paired recordings was determined by the delay between the peak of the presynaptic action potential and the onset of the EPSP. The onset was determined by the projection of the intersection of two linear fits on the postsynaptic signal (*69*). The first line was fitted to the baseline 2 ms window from -1 to +1 ms of the presynaptic AP peak. The second line was fitted on the rising phase of the EPSP (5-30% of the amplitude). The time point of the crossing lines was projected back to the signal and it was used as the onset (Fig. 2B). For the forward propagation dendritic experiments the onset of the current injection evoked EPSP-like potentials was determined by experts due to the low signal to noise ratio of the somatic channel.
The bAP latency was measured at the half-amplitude of the signals (*70*). Only the first APs of the sweeps were analyzed to avoid activity dependent Na^+ channel inactivation that can cause a putative modulatory effect on the signal propagation speed. For the axon bleb recordings we assumed that the axon initial segment of the cells are 35 um from the axon hillock, and the APs propagate to forward (to the bleb) and backward (to the soma) at the same speed.

Estimating passive parameters of L2/3 pyramidal cells

We constructed detailed passive compartmental and cable models for five L2/3 human neurons and the two mouse L2/3 neurons that were both 3D morphologically reconstructed and biophysically characterized. For each modeled neuron, we optimized the values of three key

passive parameters: the specific membrane resistivity and capacitance (R_m, C_m) and the specific axial resistivity, R_a, using Neuron 8.0 (*71*) principal axis optimization algorithm (*72, 73*). Optimization was achieved by minimizing the difference between experimental voltage response following hyperpolarizing current steps either to the soma or to the apical dendrite (Fig 8A,B) and the model response. When possible, experimental data was averaged over repetitions of the same stimulus.

To account for the surface area of spines, we used the spine correction factor (F) of 1.9 and 1.5 for human and rat PCs, respectively, by multiplying C_m and dividing R_m by F in segments which are at a distance of at least 60 mm from the soma (*25, 74*). In this study we did not attempt to fit the nonlinear effect of Ih of the voltage response of the cells.

As our experimental data contains simultaneous soma-dendritic pair recordings/stimulation, we decided to fit the voltage response in one location (e.g., the soma) for the current injection in the other location (e.g., dendrites). This is a cleaner way compared to the typical case when only one recording/stimulating electrode is available, as the problem of bridge balance at the current input site does not exist in this case. As we have two recording and simulation sites, we also examined how well the model predicts the local voltage response at the injection site (Fig 8B). Analysis and simulation were conducted using Python 3.8 and visualization using matplotlib 3.15 (*75*) and seaborn 0.11 (*76*).

Modeling EPSP propagation delay and velocity

We used the NEURON simulator (*71*) to model the seven 3D reconstructed neurons (Suppl Fig. 6). To compute EPSP's propagation latency and velocity, we simulated EPSPs by injecting a brief transient alpha-shaped current, I_α, delivered either to the soma or in various dendritic loci along the modeled apical tree.

$$I_\alpha = A\left(1 - e^{\frac{-t}{\tau_0}}\right) - \left(1 - e^{\frac{-t}{\tau_1}}\right) \qquad (2)$$

where $A = 1.5$, $\tau_0 = 0.25$ and $\tau_1 = 1ms$, resulting in EPSP peak time, $t_{peak} = 0.5ms$ and peak current of $I_{peak} = 1.4nA$.

Latency of the resultant EPSP was calculated as the difference between the EPSP peak at all dendritic branches and its resulting EPSP at the soma; using a sampling time bin of 0.01ms. Velocity was calculated as the distance of the input site from soma divided by latency between these two points. Each dot in Figures 7 and 8 is the respective value for a specific dendritic segment in a specific branch of a neuron's apical tree. For each measured feature (radius, and velocity), an inset (zoom-in) matching the experimental distance range was added. It shows the average value across dendritic branches with a given distance from the soma, as a function of distance from soma, smoothed with a rolling 10 µm window. For normalizing the path distance of a given dendritic site to the soma in cable units, we calculated the space constant $\lambda = \sqrt{d\,R_m/4\,R_a}$), for each dendritic segment (where d is the segment's diameter). We then summed up the cable lengths of all segments along the path from the dendritic location to the soma. Time was normalized by the membrane time constant $\tau = R_m * C_m$. Note that, for segments far enough from cable boundary conditions and stimulus location, velocity approximately equals the theoretical value of $2\lambda/\tau$, (*27*) see Suppl Fig. 5). Hence, in the uniform case where all specific parameters are

equal for all cell modeled (Fig 7), normalizing the distance in cable should equalize latency/velocity differences resulting from diameter differences.

To account for brain tissue shrinkage due to fixation, for every segment, diameter and length were scaled based on an estimation of specific neuron shrinkage (see Suppl. Table 1). To account for unequal dye spread, for a few manually picked segments, diameter value was fixed to be equal to its nearby segment (to avoid sudden diameter jump).

To account for brain tissue shrinkage due to fixation, for every segment, diameter and length were scaled based on an estimation of specific neuron shrinkage (see Suppl. Table 1). To account for unequal dye spread, for a few manually picked segments, diameter value was fixed to be equal to its nearby segment.

Statistical Analysis

Data presented as the mean ± s.d. Normality was tested with the Shapiro-Wilk test. For statistical analysis, t-test, Mann-Whitney U -test or Wilcoxon signed-rank test was used. Correlations were tested using Spearman's correlation, respectively. The data are shown as the median with mean, the interquartile range (of lower and upper quartile) and outlier range (±1.5 IQR) unless stated otherwise. Differences were accepted as significant if $p < 0.05$.

References

1. N. A. Oberheim, T. Takano, X. Han, W. He, J. H. C. Lin, F. Wang, Q. Xu, J. D. Wyatt, W. Pilcher, J. G. Ojemann, B. R. Ransom, S. A. Goldman, M. Nedergaard, Uniquely Hominid Features of Adult Human Astrocytes. *Journal of Neuroscience*. **29**, 3276–3287 (2009).
2. E. Boldog, T. E. Bakken, R. D. Hodge, M. Novotny, B. D. Aevermann, J. Baka, S. Bordé, J. L. Close, F. Diez-Fuertes, S. L. Ding, N. Faragó, Á. K. Kocsis, B. Kovács, Z. Maltzer, J. M. McCorrison, J. A. Miller, G. Molnár, G. Oláh, A. Ozsvár, M. Rózsa, S. I. Shehata, K. A. Smith, S. M. Sunkin, D. N. Tran, P. Venepally, A. Wall, L. G. Puskás, P. Barzó, F. J. Steemers, N. J. Schork, R. H. Scheuermann, R. S. Lasken, E. S. Lein, G. Tamás, Transcriptomic and morphophysiological evidence for a specialized human cortical GABAergic cell type. *Nat Neurosci*. **21**, 1185–1195 (2018).
3. I. Ballesteros Yáñez, A. Muñoz, J. Contreras, J. Gonzalez, E. Rodriguez-Veiga, J. DeFelipe, Double bouquet cell in the human cerebral cortex and a comparison with other mammals. *Journal of Comparative Neurology*. **486**, 344–360 (2005).
4. J. Berg, S. A. Sorensen, J. T. Ting, J. A. Miller, T. Chartrand, A. Buchin, T. E. Bakken, A. Budzillo, N. Dee, S. L. Ding, N. W. Gouwens, R. D. Hodge, B. Kalmbach, C. Lee, B. R. Lee, L. Alfiler, K. Baker, E. Barkan, A. Beller, K. Berry, D. Bertagnolli, K. Bickley, J. Bomben, T. Braun, K. Brouner, T. Casper, P. Chong, K. Crichton, R. Dalley, R. de Frates, T. Desta, S. D. Lee, F. D'Orazi, N. Dotson, T. Egdorf, R. Enstrom, C. Farrell, D. Feng, O. Fong, S. Furdan, A. A. Galakhova, C. Gamlin, A. Gary, A. Glandon, J. Goldy, M. Gorham, N. A. Goriounova, S. Gratiy, L. Graybuck, H. Gu, K. Hadley, N. Hansen, T. S. Heistek, A. M. Henry, D. B. Heyer, D. J. Hill, C. Hill, M. Hupp, T. Jarsky, S. Kebede, L. Keene, L. Kim, M. H. Kim, M. Kroll, C. Latimer, B. P. Levi, K. E. Link, M. Mallory, R. Mann, D. Marshall, M. Maxwell, M. McGraw, D. McMillen, E. Melief, E. J. Mertens, L. Mezei, N. Mihut, S. Mok, G. Molnar, A. Mukora, L. Ng, K. Ngo, P. R. Nicovich, J. Nyhus, G. Olah, A. Oldre, V. Omstead, A. Ozsvar, D. Park, H. Peng, T. Pham, C. A. Pom, L. Potekhina, R. Rajanbabu, S. Ransford, D. Reid, C. Rimorin, A. Ruiz, D. Sandman, J. Sulc, S. M. Sunkin, A. Szafer, V. Szemenyei, E. R. Thomsen, M. Tieu, A. Torkelson, J. Trinh, H. Tung, W. Wakeman, F. Waleboer, K. Ward, R. Wilbers, G. Williams, Z. Yao, J. G. Yoon, C. Anastassiou, A. Arkhipov, P. Barzo, A. Bernard, C. Cobbs, P. C. de Witt Hamer, R. G. Ellenbogen, L. Esposito, M. Ferreira, R. P. Gwinn, M. J. Hawrylycz, P. R. Hof, S. Idema, A. R. Jones, C. D. Keene, A. L. Ko, G. J. Murphy, L. Ng, J. G. Ojemann, A. P. Patel, J. W. Phillips, D. L. Silbergeld, K. Smith, B. Tasic, R. Yuste, I. Segev, C. P. J. de Kock, H. D. Mansvelder, G. Tamas, H. Zeng, C. Koch, E. S. Lein, Human neocortical expansion involves glutamatergic neuron diversification. *Nature*. **598**, 151–158 (2021).

5. Y. Deitcher, G. Eyal, L. Kanari, M. B. Verhoog, G. A. Atenekeng Kahou, H. D. Mansvelder, C. P. J. de Kock, I. Segev, Comprehensive Morpho-Electrotonic Analysis Shows 2 Distinct Classes of L2 and L3 Pyramidal Neurons in Human Temporal Cortex. *Cerebral Cortex*. **27**, 5398–5414 (2017).
6. G. Molnár, M. Rózsa, J. Baka, N. Holderith, P. Barzó, Z. Nusser, G. Tamás, Human pyramidal to interneuron synapses are mediated by multi-vesicular release and multiple docked vesicles. *Elife*. **5**, 1–12 (2016).
7. L. Beaulieu-Laroche, E. H. S. Toloza, M. S. van der Goes, M. Lafourcade, D. Barnagian, Z. M. Williams, E. N. Eskandar, M. P. Frosch, S. S. Cash, M. T. Harnett, Enhanced Dendritic Compartmentalization in Human Cortical Neurons. *Cell*. **175**, 643-651.e14 (2018).
8. L. Beaulieu-Laroche, N. J. Brown, M. Hansen, E. H. S. Toloza, J. Sharma, Z. M. Williams, M. P. Frosch, G. R. Cosgrove, S. S. Cash, M. T. Harnett, Allometric rules for mammalian cortical layer 5 neuron biophysics. *Nature*. **600**, 274–278 (2021).
9. A. Gidon, T. A. Zolnik, P. Fidzinski, F. Bolduan, A. Papoutsi, P. Poirazi, M. Holtkamp, I. Vida, M. E. Larkum, Dendritic action potentials and computation in human layer 2/3 cortical neurons. *Science*. **367**, 83–87 (2020).
10. B. E. Kalmbach, A. Buchin, B. Long, J. Close, A. Nandi, J. A. Miller, T. E. Bakken, R. D. Hodge, P. Chong, R. de Frates, K. Dai, Z. Maltzer, P. R. Nicovich, C. D. Keene, D. L. Silbergeld, R. P. Gwinn, C. Cobbs, A. L. Ko, J. G. Ojemann, C. Koch, C. A. Anastassiou, E. S. Lein, J. T. Ting, h-Channels Contribute to Divergent Intrinsic Membrane Properties of Supragranular Pyramidal Neurons in Human versus Mouse Cerebral Cortex. *Neuron*. **100**, 1194-1208.e5 (2018).
11. M. B. Verhoog, N. A. Goriounova, J. Obermayer, J. Stroeder, J. J. Johannes Hjorth, G. Testa-Silva, J. C. Baayen, C. P. J. de Kock, R. M. Meredith, H. D. Mansvelder, Mechanisms underlying the rules for associative plasticity at adult human neocortical synapses. *Journal of Neuroscience*. **33**, 17197–17208 (2013).
12. G. Molnár, S. Oláh, G. Komlósi, M. Füle, J. Szabadics, C. Varga, P. Barzó, G. Tamás, Complex events initiated by individual spikes in the human cerebral cortex. *PLoS Biol*. **6**, 1842–1849 (2008).
13. G. Komlósi, G. Molnár, M. Rózsa, S. Oláh, P. Barzó, G. Tamás, Fluoxetine (Prozac) and serotonin act on excitatory synaptic transmission to suppress single layer 2/3 pyramidal neuron-triggered cell assemblies in the human prefrontal cortex. *Journal of Neuroscience*. **32**, 16369–16378 (2012).
14. V. Szegedi, M. Paizs, E. Csakvari, G. Molnar, P. Barzo, G. Tamas, K. Lamsa, Plasticity in Single Axon Glutamatergic Connection to GABAergic Interneurons Regulates Complex Events in the Human Neocortex. *PLoS Biol*. **14**, 1–21 (2016).
15. N. A. Goriounova, D. B. Heyer, R. Wilbers, M. B. Verhoog, M. Giugliano, C. Verbist, J. Obermayer, A. Kerkhofs, H. Smeding, M. Verberne, S. Idema, J. C. Baayen, A. W. Pieneman, C. P. J. de Kock, M. Klein, H. D. Mansvelder, Large and fast human pyramidal neurons associate with intelligence. *Elife*. **7** (2018), doi:10.7554/ELIFE.41714.
16. H. Mohan, M. B. Verhoog, K. K. Doreswamy, G. Eyal, R. Aardse, B. N. Lodder, N. A. Goriounova, B. Asamoah, A. B. C. B. Brakspear, C. Groot, S. van der Sluis, G. Testa-Silva, J. Obermayer, Z. S. R. M. Boudewijns, R. T. Narayanan, J. C. Baayen, I. Segev, H. D. Mansvelder, C. P. J. de Kock, Dendritic and axonal architecture of individual pyramidal neurons across layers of adult human neocortex. *Cerebral Cortex*. **25**, 4839–4853 (2015).
17. R. Benavides-Piccione, M. Regalado-Reyes, I. Fernaud-Espinosa, A. Kastanauskaite, S. Tapia-González, G. León-Espinosa, C. Rojo, R. Insausti, I. Segev, J. Defelipe, Differential Structure of Hippocampal CA1 Pyramidal Neurons in the Human and Mouse. *Cereb Cortex*. **30**, 730–752 (2020).
18. S. Loomba, J. Straehle, V. Gangadharan, N. Heike, A. Khalifa, A. Motta, N. Ju, M. Sievers, J. Gempt, H. S. Meyer, M. Helmstaedter, Connectomic comparison of mouse and human cortex. *Science (1979)*. **377** (2022), doi:10.1126/SCIENCE.ABO0924/SUPPL_FILE/SCIENCE.ABO0924_MDAR_REPRODUCIBILITY_CHECKLIST.PDF.
19. A. Shapson-Coe, M. Januszewski, D. R. Berger, A. Pope, Y. Wu, T. Blakely, R. L. Schalek, P. Li, S. Wang, J. Maitin-Shepard, N. Karlupia, S. Dorkenwald, E. Sjostedt, L. Leavitt, D. Lee, L. Bailey, A. Fitzmaurice, R. Kar, B. Field, H. Wu, J. Wagner-Carena, D. Aley, J. Lau, Z. Lin, D. Wei, H. Pfister, A. Peleg, V. Jain, J. W. Lichtman, *bioRxiv*, in press, doi:10.1101/2021.05.29.446289.
20. P. Vetter, A. Roth, M. Häusser, Propagation of action potentials in dendrites depends on dendritic morphology. *J Neurophysiol*. **85**, 926–937 (2001).
21. G. Buzsáki, N. Logothetis, W. Singer, Scaling Brain Size, Keeping Timing: Evolutionary Preservation of Brain Rhythms. *Neuron*. **80**, 751–764 (2013).
22. S. B. Laughlin, T. J. Sejnowski, Communication in Neuronal Networks. *Science*. **301**, 1870 (2003).
23. G. B. West, J. H. Brown, B. J. Enquist, A general model for the origin of allometric scaling laws in biology. *Science*. **276**, 122–126 (1997).
24. G. J. Stuart, B. Sakmann, Active propagation of somatic action potentials into neocortical pyramidal cell dendrites. *Nature*. **367**, 69–72 (1994).

25. G. Eyal, M. B. Verhoog, G. Testa-Silva, Y. Deitcher, J. C. Lodder, R. Benavides-Piccione, J. Morales, J. DeFelipe, C. P. J. de Kock, H. D. Mansvelder, I. Segev, Unique membrane properties and enhanced signal processing in human neocortical neurons. *Elife*. **5**, 1–18 (2016).
26. J. J. B. Jack, D. Noble, R. W. Tsien, *Electric current flow in excitable cells* (Clarendon Press , Oxford, 1975).
27. H. Agmon-Snir, I. Segev, Signal delay and input synchronization in passive dendritic structures. *J Neurophysiol*. **70**, 2066–2085 (1993).
28. S. Herculano-Houzel, Not all brains are made the same: new views on brain scaling in evolution. *Brain Behav Evol*. **78**, 22–36 (2011).
29. J. DeFelipe, The evolution of the brain, the human nature of cortical circuits, and intellectual creativity. *Front Neuroanat*. **5** (2011), doi:10.3389/FNANA.2011.00029.
30. A. A. Galakhova, S. Hunt, R. Wilbers, D. B. Heyer, C. P. J. de Kock, H. D. Mansvelder, N. A. Goriounova, Evolution of cortical neurons supporting human cognition. *Trends Cogn Sci* (2022), doi:10.1016/J.TICS.2022.08.012.
31. S. R. y. Cajal, Estudios sobre la corteza cerebral humana. *Corteza Vis Rev Trim Microgr*. **4**, 1–63 (1899).
32. Y. Manor, C. Koch, I. Segev, Effect of geometrical irregularities on propagation delay in axonal trees. *Biophys J*. **60**, 1424–1437 (1991).
33. P. Desai-Chowdhry, A. Brummer, V. Savage, *bioRxiv*, in press, doi:10.1101/2021.07.15.452445.
34. H. Cuntz, F. Forstner, A. Borst, M. Häusser, One rule to grow them all: A general theory of neuronal branching and its practical application. *PLoS Comput Biol*. **6** (2010), doi:10.1371/journal.pcbi.1000877.
35. D. B. Chklovskii, Optimal Sizes of Dendritic and Axonal Arbors in a Topographic Projection. *J Neurophysiol*. **83**, 2113–2119 (2000).
36. W. Rall, "Theoretical significance of dendritic trees and motoneuron input-output relations" in *Neural Theory and Modeling*, R. F. Reiss, Ed. (Palo Alto: Stanford University Press, 1964), pp. 122–146.
37. S. S. H. Wang, W. Denk, M. Häusser, Coincidence detection in single dendritic spines mediated by calcium release. *Nat Neurosci*. **3**, 1266–1273 (2000).
38. C. J. Roome, B. Kuhn, Simultaneous dendritic voltage and calcium imaging and somatic recording from Purkinje neurons in awake mice. *Nat Commun*. **9**, 1–14 (2018).
39. H. Agmon-Snir, C. E. Carr, J. Rinzel, The role of dendrites in auditory coincidence detection. *Nature*. **393**, 268–272 (1998).
40. E. Hay, A. Gidon, M. London, I. Segev, G. Stuart, N. Spruston, M. Häusser, Eds., A theoretical view of the neuron as an input–output computing device. *Dendrites* (2016), pp. 439–464.
41. D. Dalügge, S. Remy, Human Cortical Dendrites: Stretched to Perform Better? *Cell*. **175**, 635–637 (2018).
42. M. Fişek, M. Häusser, Are Human Dendrites Different? *Trends Cogn Sci*. **24**, 411–412 (2020).
43. M. London, M. Häusser, Dendritic Computation. *Annu Rev Neurosci*. **28**, 503–532 (2005).
44. N. Spruston, G. Stuart, M. Häusser, Principles of dendritic integration. *Dendrites*, 351–398 (2016).
45. L. Campagnola, S. C. Seeman, T. Chartrand, L. Kim, A. Hoggarth, C. Gamlin, S. Ito, J. Trinh, P. Davoudian, C. Radaelli, M. H. Kim, T. Hage, T. Braun, L. Alfiler, J. Andrade, P. Bohn, R. Dalley, A. Henry, S. Kebede, A. Mukora, D. Sandman, G. Williams, R. Larsen, C. Teeter, T. L. Daigle, K. Berry, N. Dotson, R. Enstrom, M. Gorham, M. Hupp, S. D. Lee, K. Ngo, P. R. Nicovich, L. Potekhina, S. Ransford, A. Gary, J. Goldy, D. McMillen, T. Pham, M. Tieu, L. Siverts, M. Walker, C. Farrell, M. Schroedter, C. Slaughterbeck, C. Cobb, R. Ellenbogen, R. P. Gwinn, C. D. Keene, A. L. Ko, J. G. Ojemann, D. L. Silbergeld, D. Carey, T. Casper, K. Crichton, M. Clark, N. Dee, L. Ellingwood, J. Gloe, M. Kroll, J. Sulc, H. Tung, K. Wadhwani, K. Brouner, T. Egdorf, M. Maxwell, M. McGraw, C. A. Pom, A. Ruiz, J. Bomben, D. Feng, N. Hejazinia, S. Shi, A. Szafer, W. Wakeman, J. Phillips, A. Bernard, L. Esposito, F. D. D'Orazi, S. Sunkin, K. Smith, B. Tasic, A. Arkhipov, S. Sorensen, E. Lein, C. Koch, G. Murphy, H. Zeng, T. Jarsky, Local connectivity and synaptic dynamics in mouse and human neocortex. *Science (1979)*. **375** (2022), doi:10.1126/science.abj5861.
46. D. O. Hebb, *The Organization of Behavior* (John Wiley and Sons, New York, 1949).
47. T. Bliss, G. Collingridge, Persistent memories of long-term potentiation and the N-methyl-d-aspartate receptor. *Brain Neurosci Adv*. **3**, 239821281984821 (2019).
48. R. C. Malenka, M. F. Bear, LTP and LTD: An embarrassment of riches. *Neuron*. **44**, 5–21 (2004).
49. D. M. Kullmann, A. W. Moreau, Y. Bakiri, E. Nicholson, Plasticity of Inhibition. *Neuron*. **75**, 951–962 (2012).
50. D. Debanne, Y. Inglebert, M. Russier, Plasticity of intrinsic neuronal excitability. *Curr Opin Neurobiol*. **54**, 73–82 (2019).
51. H. Markram, W. Gerstner, P. J. Sjöström, Spike-timing-dependent plasticity: a comprehensive overview. *Front Synaptic Neurosci*. **4** (2012), doi:10.3389/FNSYN.2012.00002.
52. Y. Dan, M. M. Poo, Spike timing-dependent plasticity of neural circuits. *Neuron*. **44**, 23–30 (2004).
53. H. D. Mansvelder, M. B. Verhoog, N. A. Goriounova, Synaptic plasticity in human cortical circuits: cellular mechanisms of learning and memory in the human brain? *Curr Opin Neurobiol*. **54**, 186–193 (2019).

54. R. Chittajallu, K. Auville, V. Mahadevan, M. Lai, S. Hunt, D. Calvigioni, K. A. Pelkey, K. A. Zaghloul, C. J. McBain, Activity-dependent tuning of intrinsic excitability in mouse and human neurogliaform cells. *Elife*. **9**, 1–30 (2020).
55. N. Caporale, Y. Dan, Spike timing-dependent plasticity: A Hebbian learning rule. *Annu Rev Neurosci*. **31**, 25–46 (2008).
56. H. Markram, J. Lübke, M. Frotscher, B. Sakmann, Regulation of synaptic efficacy by coincidence of postsynaptic APs and EPSPs. *Science (1979)*. **275**, 213–215 (1997).
57. D. E. Feldman, The Spike-Timing Dependence of Plasticity. *Neuron*. **75**, 556–571 (2012).
58. G. Q. Bi, M. M. Poo, Synaptic modifications in cultured hippocampal neurons: Dependence on spike timing, synaptic strength, and postsynaptic cell type. *Journal of Neuroscience*. **18**, 10464–10472 (1998).
59. L. M. Ward, Synchronous neural oscillations and cognitive processes. *Trends Cogn Sci*. **7**, 553–559 (2003).
60. J. G. Klinzing, N. Niethard, J. Born, Mechanisms of systems memory consolidation during sleep. *Nature Neuroscience 2019 22:10*. **22**, 1598–1610 (2019).
61. G. Buzsáki, Hippocampal sharp wave-ripple: A cognitive biomarker for episodic memory and planning. *Hippocampus*. **25**, 1073–1188 (2015).
62. G. Buzśaki, X. J. Wang, Mechanisms of gamma oscillations. *Annu Rev Neurosci*. **35**, 203–225 (2012).
63. R. G. Averkin, V. Szemenyei, S. Bordé, G. Tamás, Identified Cellular Correlates of Neocortical Ripple and High-Gamma Oscillations during Spindles of Natural Sleep. *Neuron*. **92** (2016), doi:10.1016/j.neuron.2016.09.032.
64. M. le van Quyen, L. E. Muller, B. Telenczuk, E. Halgren, S. Cash, N. G. Hatsopoulos, N. Dehghani, A. Destexhe, High-frequency oscillations in human and monkey neocortex during the wake-sleep cycle. *Proc Natl Acad Sci U S A*. **113**, 9363–9368 (2016).
65. A. P. Vaz, J. H. Wittig, S. K. Inati, K. A. Zaghloul, Replay of cortical spiking sequences during human memory retrieval. *Science (1979)*. **367**, 1131–1134 (2020).
66. M. A. Wilson, B. L. McNaughton, Reactivation of hippocampal ensemble memories during sleep. *Science (1979)*. **265**, 676–679 (1994).
67. W. E. Skaggs, B. L. McNaughton, Replay of neuronal firing sequences in rat hippocampus during sleep following spatial experience. *Science*. **271**, 1870–1873 (1996).
68. Z. Nádasdy, H. Hirase, A. Czurkó, J. Csicsvari, G. Buzsáki, Replay and time compression of recurring spike sequences in the hippocampus. *Journal of Neuroscience*. **19**, 9497–9507 (1999).
69. M. J. Fedchyshyn, L. Y. Wang, Activity-dependent changes in temporal components of neurotransmission at the juvenile mouse calyx of Held synapse. *J Physiol*. **581**, 581–602 (2007).
70. H. Hu, M. Martina, P. Jonas, Dendritic mechanisms underlying rapid synaptic activation of fast-spiking hippocampal interneurons. *Science (1979)*. **327**, 52–58 (2010).
71. M. L. Hines, A. P. Davison, E. Muller, NEURON and Python. *Front Neuroinform*. **3** (2009), doi:10.3389/NEURO.11.001.2009.
72. R. Brent, "A new algorithm for minimizing a function of several variables without calculating derivatives" in *Algorithms for Minimization without Derivatives* (Prentice Hall, Englewood Cliffs, NJ, 1976), pp. 200–248.
73. I. Segev, J. W. Fleshman, R. E. Burke, "Compartmental models of complex neurons" in *Methods in Neuronal Modeling: From Synapses to Networks* (MIT Press, Massachusetts, 1989), pp. 63–96.
74. S. Hunt, Y. Leibner, E. J. Mertens, N. Barros-Zulaica, L. Kanari, T. S. Heistek, M. M. Karnani, R. Aardse, R. Wilbers, D. B. Heyer, N. A. Goriounova, M. B. Verhoog, G. Testa-Silva, J. Obermayer, T. Versluis, R. Benavides-Piccione, P. de Witt-Hamer, S. Idema, D. P. Noske, J. C. Baayen, E. S. Lein, J. DeFelipe, H. Markram, H. D. Mansvelder, F. Schürmann, I. Segev, C. P. J. de Kock, Strong and reliable synaptic communication between pyramidal neurons in adult human cerebral cortex. *Cerebral Cortex*, 1–22 (2022).
75. J. D. Hunter, Matplotlib: A 2D graphics environment. *Comput Sci Eng*. **9**, 90–95 (2007).
76. M. L. Waskom, seaborn: statistical data visualization, doi:10.21105/joss.03021.

Acknowledgments

The authors thank Éva Tóth, Katalin Kocsis, Leona Mezei and Bettina Lehóczki for assistance in anatomical experiments, Judith Baka for providing the electron micrographs for membrane thickness measurements and Attila Ozsvár, Márton Rózsa, Martin Tóth, Ildikó Szöts, Norbert Mihut, Róbert Averkin, Sándor Bordé, Viktor Szegedi for useful feedback and suggestions. The technical help and methodical suggestions of János Szabadics, János Brunner and Viktor Oláh at the beginning of the project are appreciated.

Funding:

KKP_20 Élvonal KKP133807 (G.T.)
Ministry of Human Capacities Hungary (20391-3/2018/FEKUSTRAT) (G.T.)
National Research, Development and Innovation Office (OTKA K128863) (G.T., G.M.)
ÚNKP-21-5-SZTE-580 New National Excellence Program of the Ministry for Innovation and Technology from the source of the National Research, Development and Innovation Fund (G.M.)
ÚNKP 16-3-VIII-3 new national excellence program of the Ministry of Human Capacities (G.O.)
János Bolyai Research Scholarship of the Hungarian Academy of Sciences (G.M.)
Hungarian Scientific Research Foundation under grant ANN-135291 (ASz)

Author contributions:

Conceptualization: GT, IS, GM, GO
Methodology: GO, GM, RL, AS, PB, SS, YL, IS, GT
Investigation: GO, GM, RL, AS, PB, SS, YL
Visualization: GO, GM, SS
Supervision: GM, IS, GT
Writing—original draft: GO, SS, GM, IS, GT
Writing—review & editing: GO, SS, GM, IS, GT

Competing interests: Authors declare that they have no competing interests.

Data and materials availability: All data, code, and materials used in the analyses will be available in https://dandiarchive.org/ to any researcher for purposes of reproducing or extending the analyses following publication.

Figures and Tables

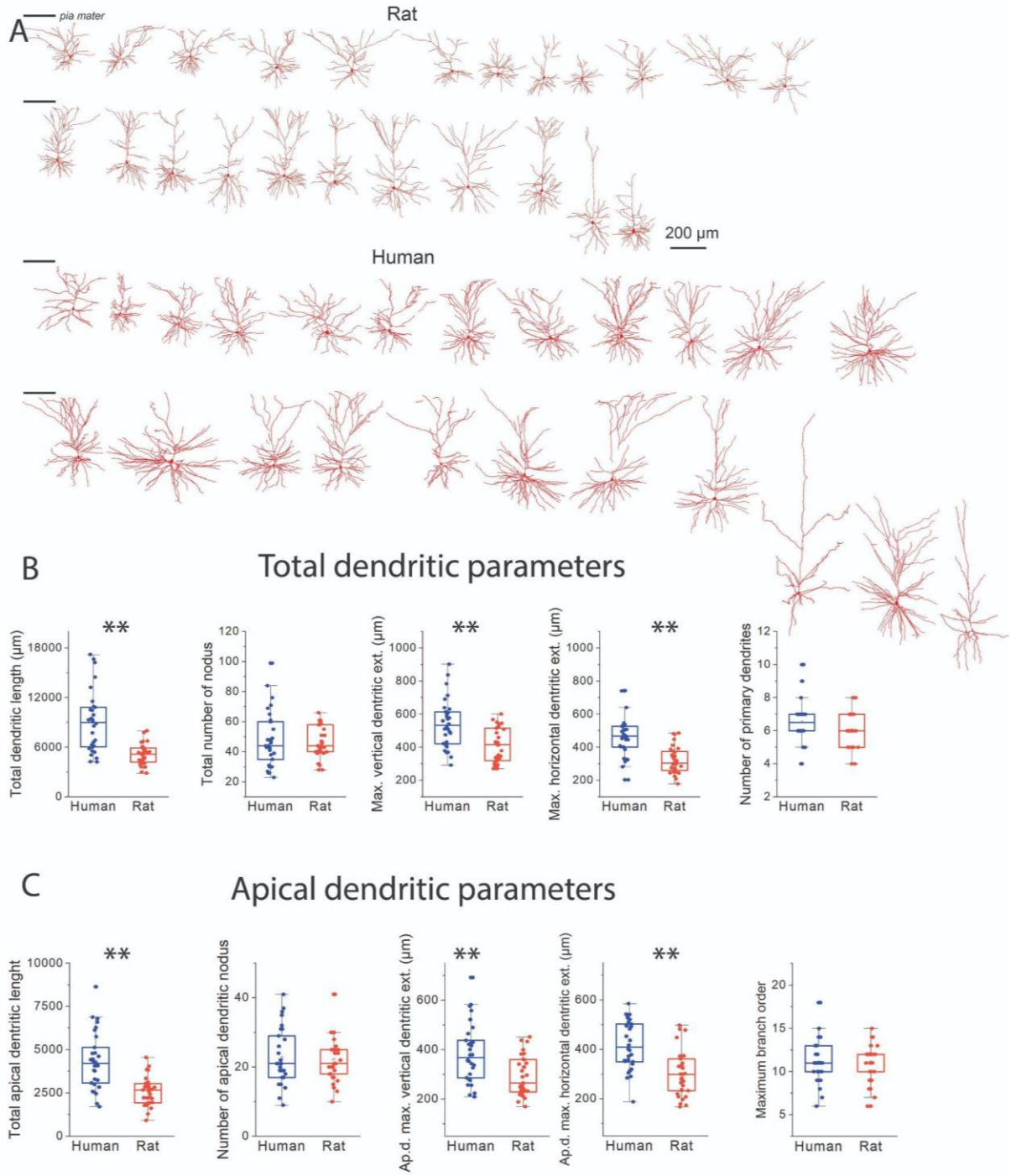

Fig. 1. Size comparison of layer 2/3 pyramidal cells in the human and rat cortex. (**A**) Sample reconstructions of fully recovered rat and human cortical pyramidal cells. Left horizontal line indicates the location of pia mater. (**B**) Comparison of dendritic length, number of nodes, maximum vertical and horizontal extension, and the number of primary dendrites respectively of all reconstructed dendritic arborization. (**C**) Comparison of length, number of nodes, maximum vertical and horizontal extension and the number of maximum branch order respectively of the apical dendrites. ** denotes significant difference $P < 0.01$

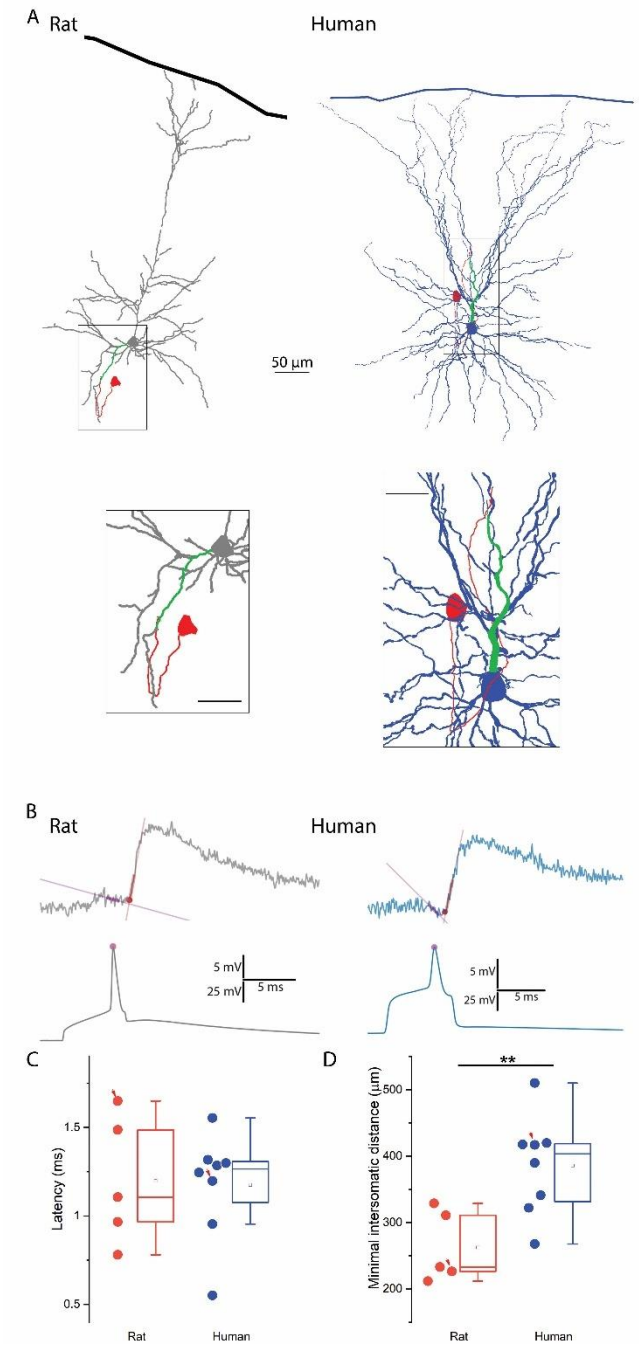

Fig.2. Paired recordings from synaptically connected layer 2/3 rat and human pyramidal cells. (**A**) Representative reconstructions of electrophysiologically recorded and biocytin filled rat (left, gray soma and dendrites) and human (right, blue soma and dendrites) synaptically connected pyramidal cell pairs. The presynaptic soma and the axon are in red; the postsynaptic dendritic path from the synapse to the soma is highlighted in green. Minimal intersomatic distance was calculated as the sum of the shortest presynaptic axonal (red) and postsynaptic dendritic (green) paths. Boxed region is magnified on the bottom. Scale bars for insets are 20 µm. (**B**) Synaptic latency was determined as the time difference between the peak of the presynaptic AP (pink dot) and the onset of the postsynaptic excitatory postsynaptic potential (red dot). Straight lines indicate baseline and rise phase fitting. (**C**) Summary of synaptic latencies in rat (red) and human (blue) cell pair recordings. There was no significant difference between the two species (rat: 1.198 ± 0.361 ms, human: 1.175 ± 0.301 ms, two-sample *t* test: P = 0.905). (**D**) Minimal intersomatic distance of the recorded cell pairs. Intersomatic distance was calculated through every putative synapse and the shortest was taken into account. The minimal intersomatic distance was significantly longer in the human (black) dataset compared to rats (blue, rat: 262.22 ± 53.639 µm, human: 385.7 ± 74.277 µm, two-sample *t* test: P = 0.008). Boxes represent median and IQR, whiskers represent outlier range (±1.5 IQR); mean is indicated by open square. The red arrowheads in C and D represent the example cell pairs shown in A.

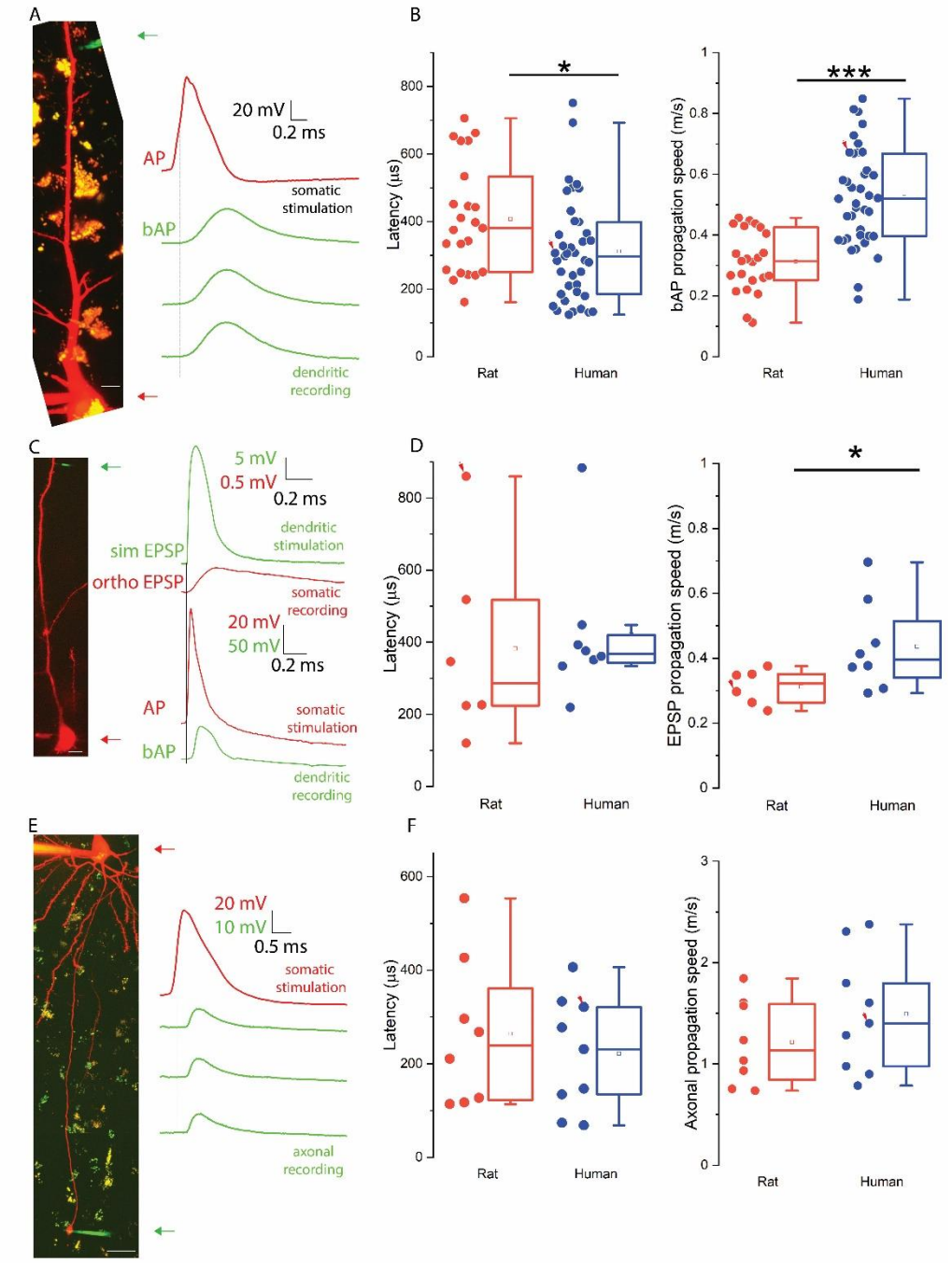

Fig. 3. Propagation velocity of dendritic and axonal signals in rat and human cortical pyramidal cells. (**A**) Left, Two-photon image of a human pyramidal cell simultaneously recorded with a somatic (red arrow) and dendritic (green arrow) electrode. Scalebar 10 µm. Right, Somatic depolarizing current evoked action potentials (red trace, average) and their backpropagation into the dendritic recording site (green traces, single sweeps) were recorded in current-clamp mode. (**B**) Left, bAP latency was shorter in human cells (rat: 407.35 ± 162.39 µs vs. human: 314.27 ± 153.97 µs, Mann-Whitney test: P = 0.0304). Right, bAP propagation speed was significantly higher in human dendrites (rat: 0.31 ± 0.1 m/s vs. human: 0.53 ± 0.16 m/s, two-sample *t* test with unequal variances: $P = 2.691 \times 10^{-8}$). Red arrowheads indicate data from cells shown on panels A and C. * P < 0.05, *** P < 0.001 (**C**) Left, Two-photon image of a rat pyramidal cell simultaneously recorded with a somatic (red arrow) and dendritic (green arrow) electrode. Scalebar 10 µm. Top, Dendritic stimulation with simulated EPSP waveform (green, average) and somatic response (red, average). Bottom, Somatic stimulation triggers an action potential (red, average) detected in the dendrite as bAP (green, average). (**D**) Left, simulated EPSP latency in human cells. Right, simulated EPSP propagation speed was significantly higher in human dendrites (rat: 0.312 ± 0.054 m/s vs. human: 0.435 ± 0.138 µs, Mann-Whitney test: P = 0.045). Red arrowheads indicate data from cells shown on panels A and C. (**E**) Left, Two-photon image of a human pyramidal cell simultaneously recorded with a somatic (red arrow) and axonal (green

arrow) electrode. Scalebar 20 µm. Right, Somatic depolarizing current evoked action potentials (red, average) and their propagation to the axonal recording site (green, single sweeps) were recorded in current-clamp mode. (**F**) Action potential propagation speed measured along the axon shows no significant difference between human and rat (rat: n = 8, 1.214 ± 0.419 m/s vs. human: n = 9, 1.492 ± 0.583 m/s, two sample *t* test: P = 0.282). Red arrowheads indicate data from cell shown on panel E.

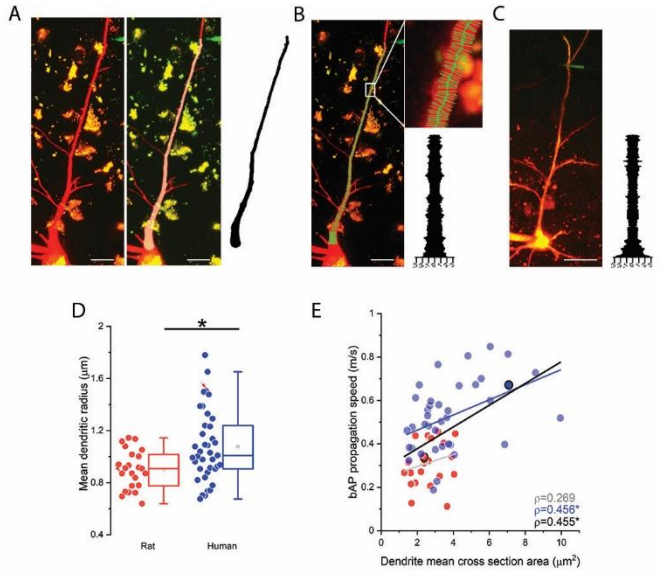

Fig. 4. Dendritic thickness reconstructions and comparison of layer 2/3 pyramidal cells in the human and rat cortex. (**A**) Left, Maximum intensity projection of Alexa594 and biocytin filled human pyramidal cell in two-photon microscope. Right, model of 3D reconstructed apical dendrite. Middle, overlay of the two-photon image and the model. (**B**) Apical dendrite thickness measurements on the sample shown in A. Left, The center of the dendrite is tracked by a thick green line while the perpendicular thin lines show measured profiles. Right, Stacked thickness measurements with micrometer scale. (**C**) Same as in B with a rat sample. Scalebars 20 µm. (**D**) Comparison of n = 23 rat (red) and n = 39 (blue) human apical dendrite averaged thickness. Red arrows indicate data measured on image stacks shown in panel B and C. P < 0.05. (**E**) bAP propagation speed correlates significantly with dendrite thickness. Spearman correlation coefficient values for fitted lines are shown on the bottom right of the plots for rat (gray), human (blue), and pooled data (black). Asterisks represent a significant correlation of the variables. * P < 0.05. Datapoints highlighted with black outline represents the cells showed in panel B and C.

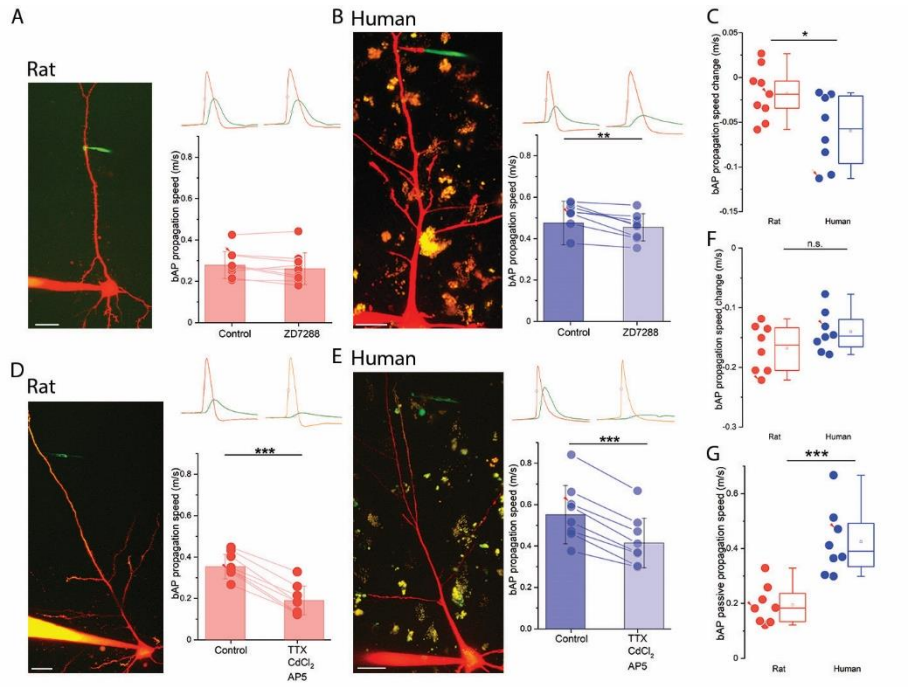

Fig. 5. Contribution of HCN, Ca^{2+}, Na^{+} and NMDA channels to bAP propagation speed in rat and human dendrites. (**A**) Representative recording from layer 2/3 pyramidal cell of a rat. Two-photon maximum intensity projection image of Alexa 594 and biocytin filled neuron on the left, representative somatic AP (red) and dendritic bAP (green) on the upper right in the control condition (left) and after 20 µM ZD7288 application (right). The bar plot shows the population average of signal propagation velocity in control conditions and after drug application (control: 0.285 ± 0.067 m/s, ZD7288: 0.267 ± 0.078 m/s, paired *t* test: P = 0.104). Red arrowhead points to data measured in the presented example cell. (**B**) Same as in panel A but for human cells (control: 0.486 ± 0.108 m/s, ZD7288: 0.466 ± 0.067 m/s, Wilcoxon signed ranks test: P = 0.014). (**C**) Changes in bAP propagation speeds from control to drug application. The blockage of HCN channels changed bAP speeds more in human compared to the rat (rat: -0.018 ± 0.029 m/s, human: -0.06 ± 0.04 m/s, two-sample *t* test: P = 0.029). Red arrowheads point to the data acquired from the representative samples in panel A and B. (**D-E**) Same as A and B but the ACSF contained 1 µM TTX, 200 µM $CdCl_2$, and 20 µM AP5 in the drug application condition (rat control: 0.3622 ± 0.061 m/s, rat TTX/$CdCl_2$/AP5: 0.194 ± 0.071 m/s, paired *t* test: P = 6.101×10^{-6}, human control: 0.565 ± 0.144 m/s, human TTX/$CdCl_2$/AP5: 0.425 ± 0.123 m/s, paired t test: P = 7.739×10^{-6}). (**F**) Changes in bAP propagation speeds from control to TTX/$CdCl_2$/AP5 application were similar in both species (rat: -0.168 ± 0.039 m/s, human: -0.14 ± 0.034 m/s, two-sample *t* test: P = 0.155). (**G**) Comparison of bAP velocities measured in the cocktail of TTX/$CdCl_2$/AP5 blockers reveals higher speed of propagation in human (rat: n = 8, 0.194 ± 0.071 m/s, human: n = 8, 0.425 ± 0.123 m/s, two sample *t* test: P = 4.244×10^{-4}). Boxes represent median and IQR, whiskers represent outlier range (±1.5 IQR); mean is indicated by open square, crosses denote minimum and maximum values. Red arrowheads point to the data acquired from the representative samples in panel D and E. Scalebars 20 µm.

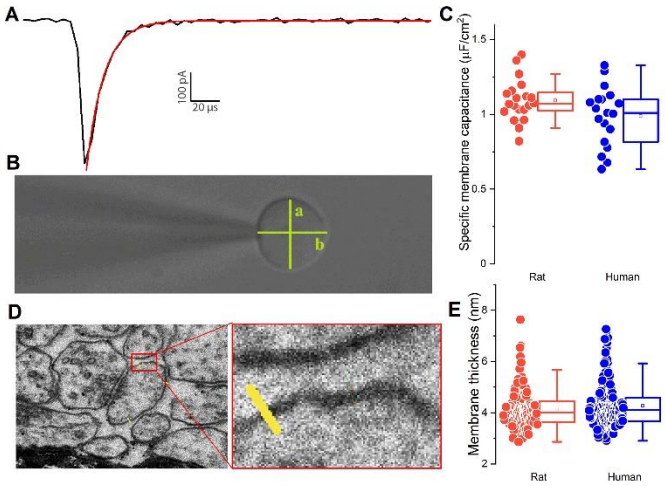

Fig. 6. Comparative analysis of membrane capacitance and thickness in rat and human cortex
(**A**) Representative capacitive transient of a nucleated patch pulled from layer 2/3 neocortical pyramidal cell (black). A single exponential function was fitted on the measured signal (red) for the calculation of the time constant of the membrane. (**B**) Differential interference contrast microscope image of a neuronal nucleus. The shortest (a) and longest (b) diameter values were used to calculate the membrane surface. (**C**) Specific membrane capacitance of rat (red, 1.092 ± 0.14 µF/cm^2, n = 20) and human (blue, 0.987 ± 0.196 µF/cm^2, n = 19, two-sample *t* test with equal variance: P = 0.0615) neocortical pyramidal cells. (**D**) Electron micrographs of dendritic membranes used for membrane thickness measurements. Yellow lines indicate measuring profiles. Boxed region magnified on the right. (**E**) Membrane thickness of rat (red, 4.122 ± 0.779 nm, n =151 from n = 3 rat) and human (blue, 4.271 ± 0.873 nm, n = 213 from n = 3 patient) neocortical cell dendrites (Mann-Whitney test: P = 0.212). Boxes represent median and IQR, whiskers represent outlier range (± 1.5 IQR); mean is indicated by open square.

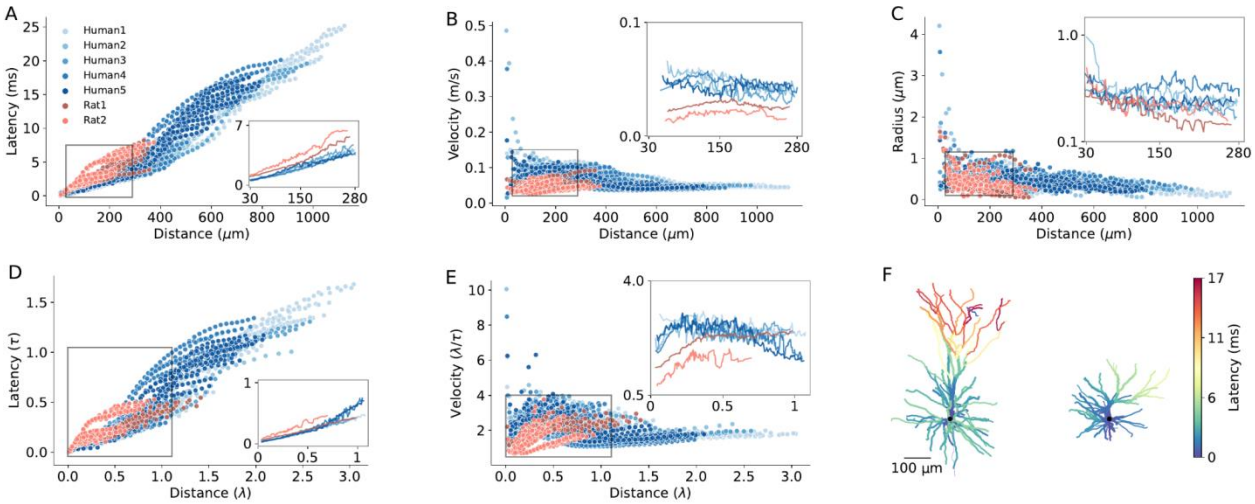

Fig. 7. Modeling EPSPs latency and velocity in dendrites of human and rat L2/3 pyramidal cells. Uniform cable parameters. (**A**) Latency and (**B**)**,** velocity of EPSP in cable models of 5 human (in blue) and 2 rats' (in red) reconstructed L2/3 PCs (see color legend in A). Insets show the respective average for the zoom-in region depicted by the box. For these computations, the specific cable properties of all 7 models were identical (C_m = 1 $\mu F/cm^2$, R_m = 15,000 Ωcm^2, R_a = 150 Ωcm). Note the smaller latency and larger velocity in human PCs. Selected zoom-in region brackets the range of distances where the experimental recordings were performed. Insets show the average of latency and velocity of all dendrites at a given distance from the soma, per cell. (**C**)**.** Dendritic radius as a function of distance from the soma for the 7 modeled cells. Note the typically larger radius of human dendrites at the zoom-in region. (**D-E**) Same as A and B but for distance normalized in cable units (thus normalizing for the differences in diameters between cells) and time normalized in units of membrane time constant, which is identical for all cells. (**F**) Expected dendritic latency for exemplars 'Human5' and 'Rat2' L2/3 PCs with cable parameters as in B.

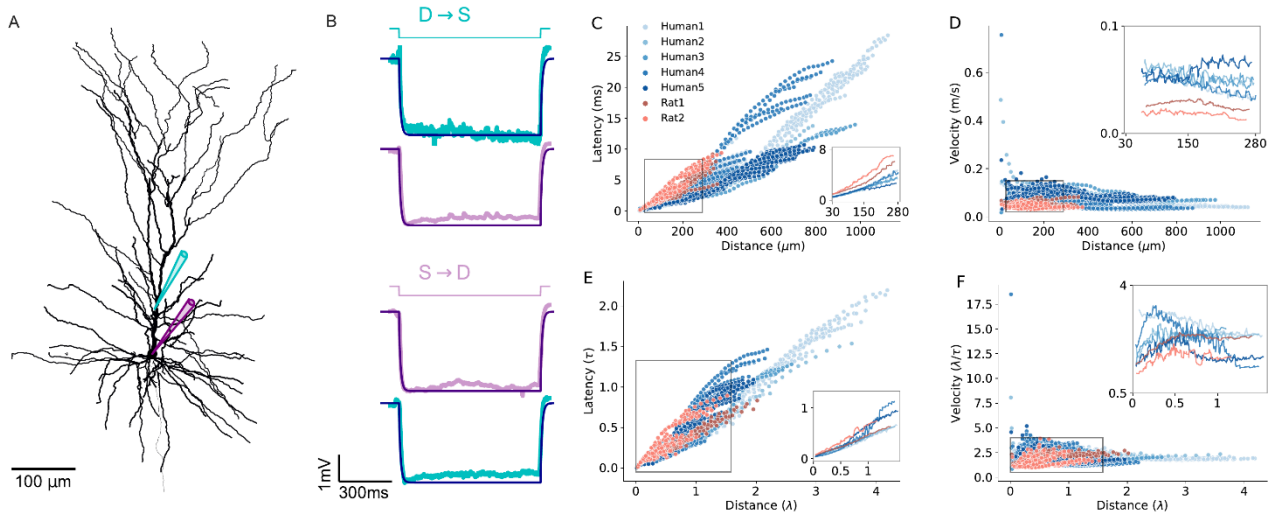

Fig. 8. Modeling EPSPs latency and velocity in dendrites of human and rat L2/3 pyramidal cells. Cable parameters fitted to experiments. (A) Exemplar modeled (Human5) neuron, including the locations of the two recording/stimulating electrodes. (**B**) **Top:** Model fit (in dark purple) to voltage response at the soma (in light purple) for steady current (-100 pA) injected to the dendrites (cyan). The resultant fit to the local dendritic voltage response (in cyan) is also shown. **Bottom:** as is Top but with current injected to the soma. This fitting procedure resulted with the following passive parameters: C_m = 0.63 $\mu F/cm^2$, R_m = 15,570 Ωcm^2, R_a = 109 Ωcm. (**C**) Latency and (**D**) Velocity of EPSPs for the 7 model cells as in Figure 7A,B, but now with specific cable parameters fitted to the individual modeled neurons (see Table **1**). Insets show the respective average for the zoom-in region depicted by the box. (**E-F**) As in B and C, with distance normalized in cable units (thus normalizing for the differences in diameters) as well as latency and velocity normalized by the membrane time constant (see Table 3). Note the smaller latency and larger velocity for the human PCs, which is now more significant as compared to the case where the cable parameters were uniform for all modeled cells as in Figure 7D and E.

Cell name	C_m ($\mu F/cm^2$)	R_m (Ωcm^2)	R_a (Ωcm)
Human1	0.65	19,875	298
Human2	0.54	16,492	298
Human3	0.85	12,872	103
Human4	0.77	21,522	209
Human5	0.63	15,570	109
Rat1	0.84	13,110	267
Rat2	1.16	9,084	249
Mean human	**0.69**	**17,266**	**203**
Mean rat	**1.00**	**11,097**	**258**

Table 1. Cable parameters fitted to experimental data. C_m and R_m are the specific membrane capacitance and resistivity, respectively; R_a is the specific axial resistance.

Cell name	d_{max} (μm)	l_{max} (μm)	L_{max}	τ(ms)	Latency (ms)
Human1	0.79	287.4	1.03	12.95	5.28
Human2	0.82	288.5	1	8.95	3.35
Human3	0.65	287.7	0.74	10.90	3.53
Human4	1.24	287.5	0.69	16.60	5.47
Human5	0.98	286.6	0.63	9.80	2.97
Rat1	0.3	287.1	1.43	11.00	7.05
Rat2	0.34	286.8	1.15	10.50	6.98
Mean human	**0.9**	**287.5**	**0.81**	**11.84**	**4.12**
Mean rat	**0.32**	**287.0**	**1.29**	**10.75**	**7.02**

Table 2. Model prediction of EPSPs latency within experimental recording distance range (27 - 288 μm from soma) per modeled cell. Cable parameters were fitted per cell as in Table 1. d_{max} and l_{max} are the maximal diameter and physical distance, respectively within the recording distance range. L_{max} is the respective distances in units of λ ($L = l/\lambda$). τ is the membrane time constant (C_m*R_m). Latency is the maximal latency measured at this distance range. All maximal values are averaged across branches, within 3μm window bin.

Supplementary Materials

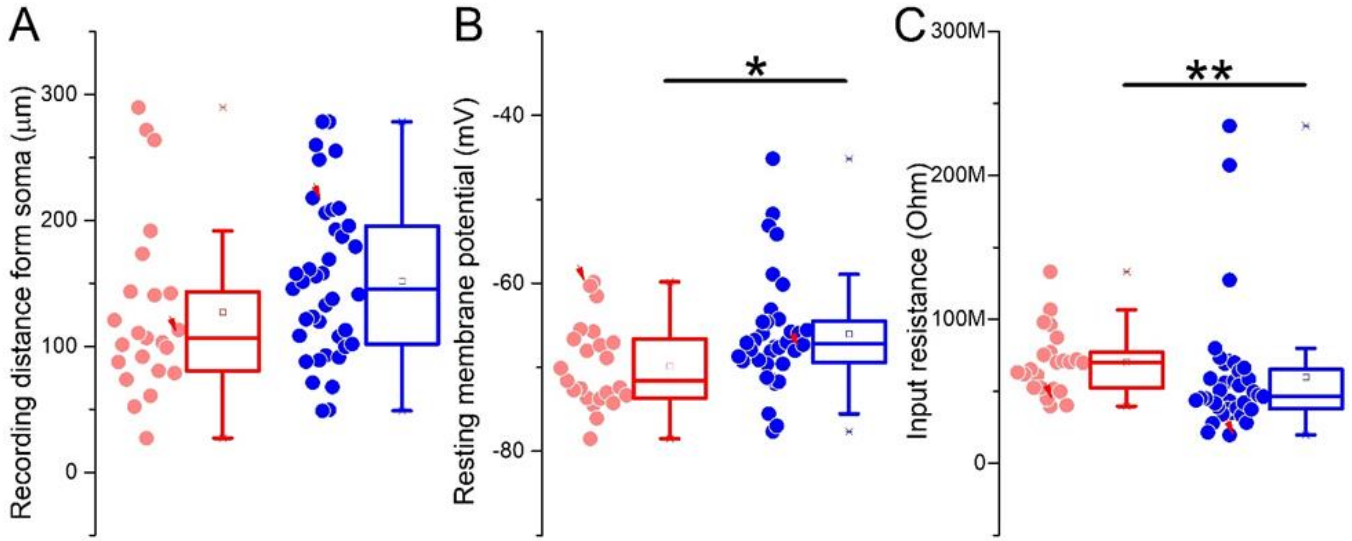

Suppl.Fig.1. Properties of dendro-somatic recording and measured membrane parameters.
(**A**) There was no significant difference between the distance of the recording sites along the dendrites in our dataset (left panel, rat: 127.06 ± 69.48 µm vs. human: 153.39 ± 62.25 µm, Mann-Whitney U test: p = 0.07543). (**B**) Resting membrane potential of the recorded cells (rat: -69.89 ± 0.50 mV, n = 23, human: -66.05 ± 0.68 mV, n=36, Mann-Whitney U test: p = 0.01854) were different in human and in rat pyramidal cells. (**C**) Input resistance of recorded cells (rat: 69.94 ± 22.56 MΩ, n = 23, human: 59.79 ± 44.35 MΩ, n = 36, Mann-Whitney U test: p= 0.00292). The red arrowheads represent the example cells shown in Fig 3A and B.

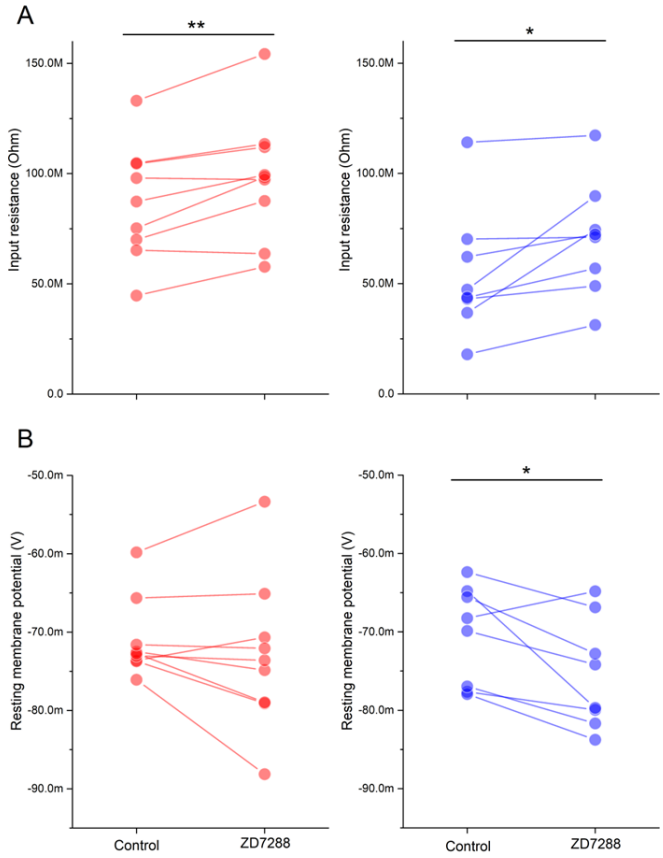

Suppl.Fig.2. Effect of ZD7288 on L2/3 PCs.
(**A**) The input resistance changed significantly in rat (red, rat control: 86.95 ± 26.34 MΩ vs rat ZD7288: 98.18 ± 28.53 MΩ, paired sample t test: P = 0.00488, n = 9) and human (blue, human control: 54.38 ± 28.8 MΩ vs human ZD7288: 70.21 ± 26.09 MΩ, paired sample t test: P = 0.02434, n = 8) after the application of 20 µM ZD7288. (**B**) Resting membrane potential of recorded cells after ZD7288 application (red, rat control: -70.98 ± 5.04 mV vs rat ZD7288: -72.88 ± 9.75 mV, Wilcoxon signed ranks test: P = 0.40694, n = 9; blue, human control: -70.43 ± 6.28 mV vs human ZD7288: -75.47 ± 6.991 mV, paired sample t test: P = 0.02682, n = 8).

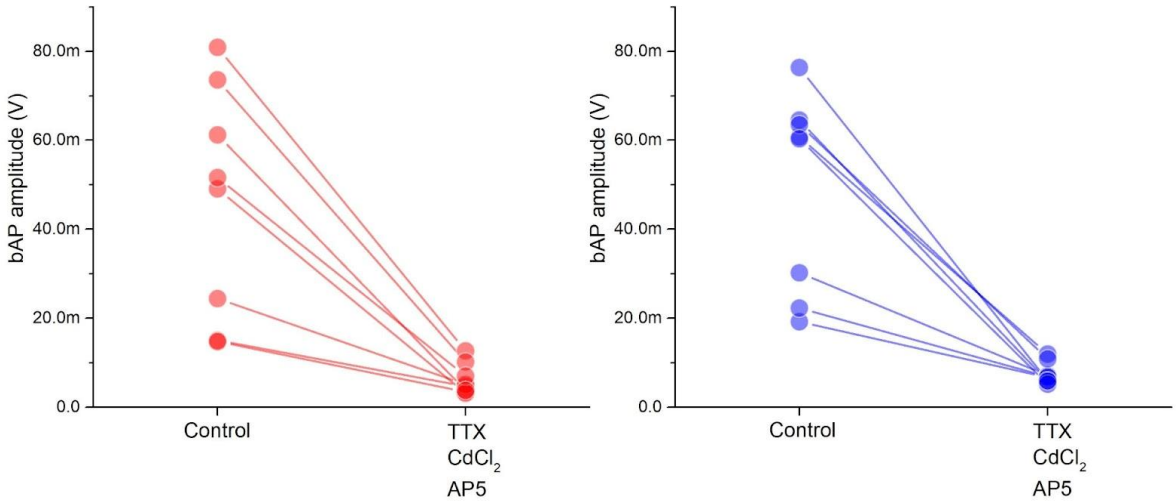

Suppl.Fig.3. Effect of voltage gated ion channel blockage on bAP amplitude.
The amplitudes of the bAPs were significantly decreased upon the application of voltage gated ion channel blockers (rat control: 46.32 ± 25.78 mV vs rat TTX, $CdCl_2$, AP5: 6.26 ± 3.47 mV, paired sample t test: P = 0.00188, n = 8, human control: 49.66 ± 22.1 mV vs. human TTX, $CdCl_2$, AP5: 7.56 ± 2.48 mV, Wilcoxon signed ranks test: P = 0.00781, n = 8).

Cell name	Length factor	Diameter factor
Human1	1.26	0.84
Human2	1.03	1.00
Human3	1.24	0.95
Human4	1.25	1.23
Human5	1.26	0.99
Rat1	1.05	1.12
Rat2	1.45	1.11

Suppl. Table 1. Morphological scaling factors due to fixation.

Cell name	l_{max} (μm)	L_{max}	Latency (ms)
Human1	288.8	0.68	3.66
Human2	288.5	0.67	3.56
Human3	288.995	0.74	4.93
Human4	288.7	0.67	4.22
Human5	287.4	0.87	5.64
Rat1	287.45	0.96	5.48
Rat2	287.186	0.68	6.3
Mean human	**288.48**	**0.73**	**4.4**
Mean rat	**287.32**	**0.82**	**5.89**

Suppl. Table 2. Model prediction of EPSPs latency within experimental recording range (27 - 288 μm) from soma) per modeled cell. Uniform cable parameters were used as in Figure 6. l_{max} is the maximal diameter and physical distance. L_{max} is the respective distances in λ units ($L = l/\lambda$). Latency is maximal latency measured at this distance range. All maximal values are averaged across branches, within 3μm window bin.

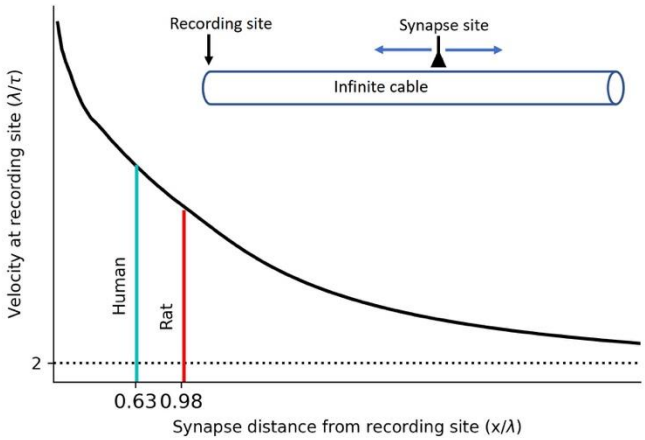

Suppl.Fig.4. Velocity of EPSP peak as a function of distance from the recording site for the case of an infinite passive cylindrical cable. Recording site is at X = 0. Note the high velocity when the synapse is near the recording site; the velocity converges to a constant value of $2\lambda/\tau$ for electrotonically distant synapses. Cyan and red lines show the maximal cable distance L_{max} (Table3) within experimental recording range of 27 - 288 μm from the soma. Cable parameters and diameter are as in Table1 and Table3 respectively, mean human and rat.

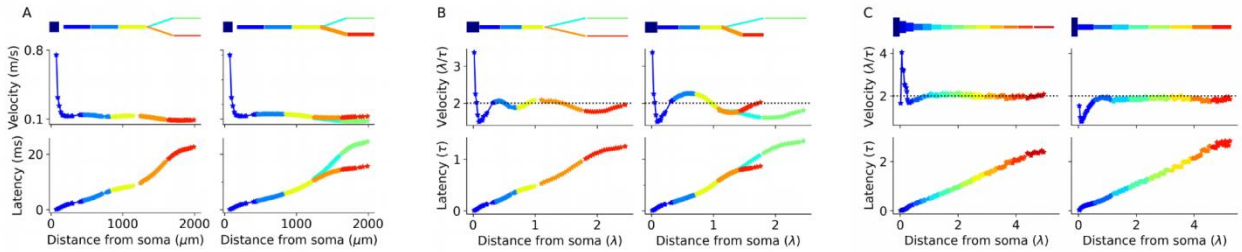

Suppl.Fig.5. Morphological irregularities affect EPSP latency and velocity. A. Cable with a single branch, with symmetrical (top left) or asymmetrical (top right) branches. Thick branches diameter is 4μm, while thin branches' diameter is 1μm. Latency and velocity were calculated as explained in the text and in Figs. 7 and 8; synaptic inputs were activated at different sites along the structure. The recording site ("soma") is at left (dark blue rectangle), with diameter of 13μm. **B.** As in A, with normalized space and time constants. For symmetrical branches, both latency and velocity overlap for the two branches (left column in both **A** and **B**), while in asymmetrical case, the latency from the thick branch is smaller as it is electrotonically closer to the soma and, therefore, for the same physical distance the initial velocity of the EPSP at its site of origin is larger (right column in **B,** red branch compared with green). However, there is a small increase in latency (decrease in velocity at these daughter branches) due to local impedance mismatch. **C**. Cable with diameters replicating the apical main-branch of 'Human2' (left column) and 'Rat1' (right column) PCs. Note the local irregularities shifts the velocity above (left column) or below (right column) $2\lambda/\tau$ despite having identical lengths across all sections. Moreover, velocity pattern changes due to the proximity of the synapse to the soma, as a function of the cable diameters. Cable parameters are identical for all morphologies (C_m = 1.5 $\mu F/cm^2$, R_m = 10,000 Ωcm^2, R_a = 150 Ωcm).

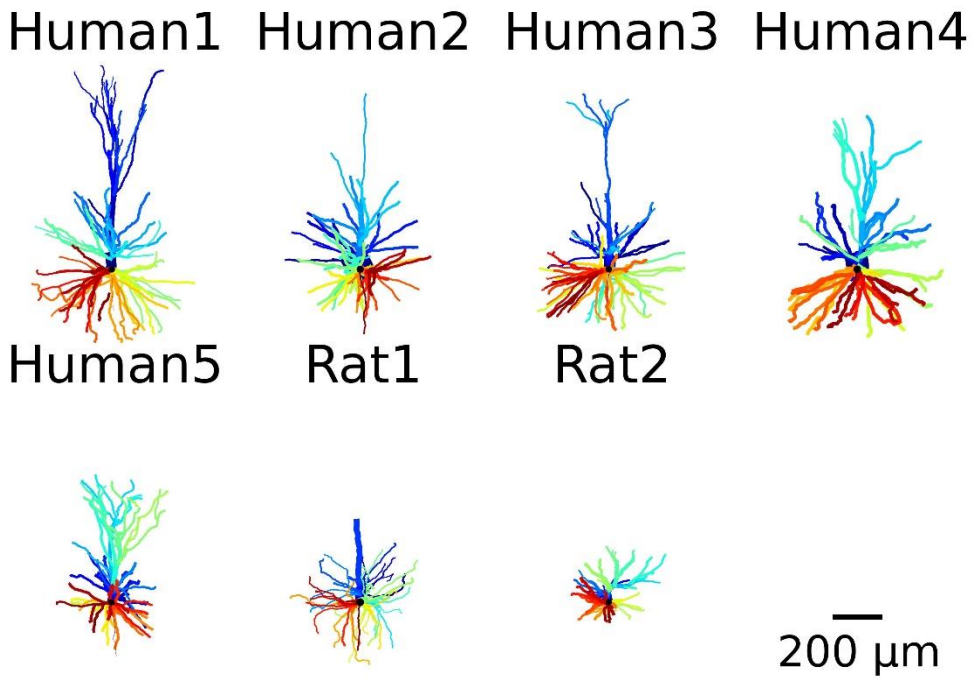

Suppl.Fig.6. Morphology of the seven modeled cells. Each section is marked by a different color.